CeO$_2$ as an "electron pump" to boost the performance of Co$_4$N in electrocatalytic hydrogen evolution, oxygen evolution and biomass oxidation valorization

Peiyun Zhou [a,1], Guangtong Hai [b,1], Gongchi Zhao [a], Rushuo Li [a], Xiubing Huang [a,*], Yunfeng Lu [c,*], Ge Wang [a,d,**]

[a] Beijing Advanced Innovation Center for Materials Genome Engineering, Beijing Key Laboratory of Function Materials for Molecule & Structure Construction, School of Materials Science and Engineering, University of Science and Technology Beijing, Beijing 100083, PR China
[b] Department of Chemical Engineering, Tsinghua University, Beijing 100084, PR China
[c] Department of Chemical and Biomolecular Engineering, University of California, Los Angeles, CA 90095, United States
[d] Shunde Graduate School, University of Science and Technology Beijing, Shunde 528399, PR China

ARTICLE INFO

ABSTRACT

Developing multifunctional electrocatalysts with excellent hydrogen evolution reaction (HER), oxygen evolution reaction (OER) and 5-hydroxymethylfurfural oxidation reaction (HMFOR) activities will contribute to "carbon neutrality". Here, CeO$_2$ is introduced into the Co$_4$N system as an "electron pump" to attract electrons to transfer from Co$_4$N to CeO$_2$. The interface electronic structure optimization enables Co$_4$N@CeO$_2$ to exhibit excellent HER, OER, and HMFOR performance. Specifically, to deliver 10 mA cm^{-2} current density, (1) it only requires low overpotentials of 49 and 263 mV for HER and OER in 1.0 M KOH, respectively; (2) it merely needs an ultra-low potential of 1.22 V$_{RHE}$ for HMFOR in 1.0 M KOH + 300 mM HMF, which is 273 mV lower than the required potential in 1.0 M KOH. Theoretical calculation results show that the introduction of CeO$_2$ effectively reduces the barriers for potential-determining steps of HER and OER, and optimizes OH$^-$ adsorption to promote the HMFOR process.

1. Introduction

Increasing reliance on traditional fossil energy has inevitably triggered environmental and energy shortage problems [1,2]. As the largest developing country, China has made a commitment to achieve "carbon neutrality" by 2060 in an environmentally responsible attitude [3]. Finding reliable alternatives to traditional fossil energy is essential for achieving "carbon neutrality" [4]. Renewable energy sources (solar energy, wind energy, etc.) have the potential to become the main components of the future energy supply system [2,5]. Using renewable electricity to produce hydrogen (H$_2$) by electrochemical methods (such as electrolysis of water) can not only obtain high-purity H$_2$ with high energy density, but also effectively solve the time-space intermittent defects of renewable electricity, so as to realize the directional

conversion and efficient storage and utilization of renewable electricity [6–8]. Electrolysis of water involves both the hydrogen evolution reaction (HER) occurring at the cathode and the oxygen evolution reaction (OER) occurring at the anode [9,10]. Typically, noble metal-based catalysts, such as Pt/C and RuO$_2$, are regarded as benchmark catalysts for HER and OER, respectively [11]. In spite of this, noble metals are too expensive and have limited reserves to be used on a large scale. The development of high-performance non-noble metal-based electrocatalysts, especially those with both high HER and high OER activities, is of great significance for realizing cost reduction of water electrolysis.

In addition, in view of the carbon-neutral nature of biomass, efficient and rational utilization of biomass is also an effective way to achieve "carbon neutrality" [12–15]. The electrochemical utilization of biomass has developed vigorously in recent years, especially with regard to the

electrochemical oxidation of 5-hydroxymethylfurfural (HMF) [13,16, 17]. On the one hand, high value-added chemicals such as 2,5-furandi-carboxylic acid (FDCA) can be obtained through the HMF oxidation reaction (HMFOR), and FDCA is regarded as an ideal substitute for terephthalic acid in industry [13]. On the other hand, coupling HMFOR with HER can also achieve efficient hydrogen production [18,19]. To enable the large-scale application of electrocatalytic HMFOR, the development of high-performance non-noble metal-based electro-catalysts is a necessary prerequisite [20]. Designing electrocatalysts with not only high HMFOR activity but also high HER activity is critical for the efficient electrochemical utilization of HMF.

Based on the above discussion, it is very attractive to develop high-performance electrocatalytic materials with three functions of HER, OER and HMFOR, which can help achieve the goal of "carbon neutrality" from three aspects: renewable electricity utilization, clean hydrogen energy production, and biomass utilization. In recent years, non-noble metal-based electrocatalytic materials such as transition metal nitrides [21], phosphides [22,23], oxides [24], and sulfides [25] have attracted more and more attention from researchers, and have been continuously used for the development of multifunctional electrocatalysts. Among them, transition metal nitrides shine in the field of electrocatalysis because of their Pt-like electronic structure and metal-like conductivity [26,27]. In particular, Co_4N, which exhibits high activity for HER, OER, etc., has the potential to be used as a design platform for multifunctional electrocatalytic materials [28,29]. However, for pure Co_4N, limited by its own electronic structure, its electrochemical performance is not very competitive. Therefore, trying to optimize the electronic structure of Co_4N is the most fundamental method to improve its electrochemical activity. For example, Luo and co-workers designed a CoO/Co_4N het-erostructure as an excellent HER electrocatalyst. They found that syn-ergistic electron interaction between CoO and Co_4N can enhance H_2O adsorption, optimize hydrogen adsorption and promote H_{ad} diffusion [30]. Similarly, in order to optimize the electronic structure of Co_4N, excellent electrocatalytic materials such as Cr-Co_4N [31], V-Co_4N [32], and MoN/Co_4N [33] have been developed. As a rare earth oxide, ceria (CeO_2) has abundant oxygen vacancies, and has great potential for application in electrocatalysis due to its excellent affinity for oxygen-containing species [34–37]. Thus, introducing CeO_2 into the Co_4N system has the possible to adjust the electronic structure of Co_4N, and flexibly control the adsorption and desorption of oxygen-containing species by utilizing the properties of CeO_2, which may help the com-posite to achieve high activity in multifunctional electrocatalysis for HER, OER and HMFOR.

Herein, a $Co_4N@CeO_2$ heterostructure supported by nickel foam, $NF/Co_4N@CeO_2$, was successfully synthesized via a hydrothermal-impregnation-nitridation process. In the $Co_4N@CeO_2$ system, CeO_2 acts as an "electron pump", effectively attracting electrons from Co_4N and promoting charge redistribution at the heterointerface. Conse-quently, $NF/Co_4N@CeO_2$ exhibits superb HER, OER, as well as HMFOR performance in alkaline media. Specifically, it merely requires over-potentials of 49 and 263 mV to deliver a current density of 10 mA cm^{-2} for HER and OER in 1.0 M KOH, respectively. And for HMFOR in 1.0 M KOH +300 mM HMF, to supply 10 mA cm^{-2} current density, only an extremely low potential of 1.22 V$_{RHE}$ (RHE: reversible hydrogen elec-trode) is required, which is 273 mV lower than the potential required for OER (1 M KOH). Additionally, to achieve 10 mA cm^{-2} current density in a two-electrode system of $NF/Co_4N@CeO_2$ $||$ $NF/Co_4N@CeO_2$, a cell voltage of 1.33 V is required in 1.0 M KOH + 300 mM HMF, which is much lower than 1.53 V in 1.0 M KOH.

2. Experimental section

2.1. Materials

Nickel foam (NF) was purchased from Beijing Tianmei Hechuang Technology Corporation. Cerium nitrate hexahydrate ($Ce(NO_3)_3 \cdot 6H_2O$,

99.99 %) was purchased from Shanghai Titan Scientific Corporation. Sodium edetate (EDTA·4Na, $\geq$ 99.0 %) was purchased from Shanghai Titanchem Corporation. Urea ($\geq$ 99.0 %) was purchased from Sino-pharm Chemical Reagent Corporation. 5-Hydroxymethylfurfural (HMF, 99.54 %) and furan-2,5-dicarbaldehyde (DFF, 98 %) were purchased from Ark Pharma Scientific Limited. Potassium hydroxide (KOH, 95 %), cobalt nitrate hexahydrate ($Co(NO_3)_2 \cdot 6H_2O$, $\geq$98.0 %), 5-hydroxy-methyl-2-furancarboxylic acid (HMFCA, 98 %), 5-formyl-2-furancarbox-ylic acid (FFCA, >98 %), and 2,5-furandicarboxylic acid (FDCA, 98 %) were purchased from Shanghai Aladdin Biochemical Technology Corporation.

2.2. Sample preparation

2.2.1. Preparation of NF/CCH

NF/CCH was synthesized through a hydrothermal method. At first, all nickel foams (3 cm × 3.5 cm) were treated with acetone, hydro-chloric acid (2 M), and deionized water for 30 min under ultrasonic conditions, respectively, to remove surface oil and oxides. Then, Co ($NO_3)_2 \cdot 6H_2O$ (2 mmol), urea (10 mmol), and EDTA·4Na (2.5 mmol) were mixed with 36 mL deionized water under magnetic stirring until a homogeneous solution was formed. Then, the solution was poured into a 50 mL Teflon container, followed by one piece of pretreated NF was vertically placed in it. Next, the container was placed in a stainless-steel autoclave, sealed, and kept at 120 ℃ for 10 h. After cooling to room temperature, the NF was taken out, washed with deionized water and absolute ethanol several times, and dried under vacuum at 60 ℃ over-night. As a result, the NF supported cobalt carbonate hydroxide nano-sheet arrays (NF/CCH) was obtained.

2.2.2. Preparation of NF/CCH@CeO_2

$NF/CCH@CeO_2$ was prepared by an impregnation method. First, a piece of cropped NF/CCH (1 cm × 1.75 cm) was placed in a 5 mL centrifuge tube containing 3 mL of $Ce(NO_3)_3$ solution (0.1 M). Then, the centrifuge tube was placed vertically in an oven and kept at 50 °C for 6 h. After the impregnation was completed, the sample was taken out and dried in a vacuum drying oven at 60 °C, and the obtained sample was denoted as $NF/CCH@CeO_2$. Similarly, $NF/CCH@CeO_2$(1 h) and NF/ $CCH@CeO_2$(12 h) were also prepared by the above method, except that the impregnation time was changed to 1 h and 12 h, respectively.

2.2.3. Preparation of NF/Co_4N@CeO_2

$NF/Co_4N@CeO_2$ was prepared by a nitridation process. At first, NF/ $CCH@CeO_2$ and urea (1 g) were placed in a tube furnace with the latter in the upstream direction. Next, under N_2 flow, the furnace was heated to 500 ℃ with a rate of 2 ℃ min^{-1}, and kept at 500 ℃ for 2 h. Finally, the obtained sample was denoted as $NF/Co_4N@CeO_2$. Similarly, NF/ Co_4N, $NF/Co_4N@CeO_2$(1 h) and $NF/Co_4N@CeO_2$(12 h) were also pre-pared by the above method, except that the precursors were changed to NF/CCH, $NF/CCH@CeO_2$(1 h) and $NF/CCH@CeO_2$(12 h), respectively. The mass loadings of NF/Co_4N, $NF/Co_4N@CeO_2$(1 h), $NF/Co_4N@CeO_2$, and $NF/Co_4N@CeO_2$(12 h) were 4.12, 5.35, 5.81, and 6.59 mg cm^{-2}, respectively, according to the results of inductively coupled plasma optical emission spectroscopy.

2.3. Materials characterization

Micro morphologies and structures were characterized by a field emission scanning electron microscopy (FE-SEM, Hitachi SU8010, accelerating voltage: 5 kV) and a field emission transmission electron microscopy (FE-TEM, JEM-2200FS, accelerating voltage: 200 kV). Phase compositions were characterized by an X-ray diffractometer (XRD, Bruker D8 Advance diffractometer, Cu Kα1: 40 kV, 40 mA, λ = 1.5406 Å), and the scanning speed and 2θ range were set as five degrees per minute and 5 ~ 80°, respectively. Raman spectra were characterized by a Raman spectrometer (HORIBA Scientific LabRAM HR Evolution,

excitation wavelength: 532 nm). Elemental contents were characterized by an inductively coupled plasma optical emission spectroscopy (ICP-OES, Agilent 5110 ICP-OES). Electron paramagnetic resonance (EPR) spectra were characterized by a Bruker A300–10/12. Surface chemical states were characterized by an X-ray photoelectron spectroscopy (XPS, Thermo ESCALAB 250Xi) with a monochromatic Al Kα (1486.6 eV) X-ray source. XPS spectra were fitted by the software of Thermo Avantage with the L/G Mix Convolve fixed at 30 %, and all spectra were calibrated with reference to the C 1s peak (284.8 eV).

2.4. Electrochemical measurements

All electrochemical tests were performed on electrochemical work-stations (CHI 660D and PRINCETON APPLIED RESEARCH). The three-electrode system was configured as working electrode (self-supporting nickel foam electrode, effective geometric area: 1 cm × 0.5 cm), counter electrode (graphite rod) and reference electrode (Hg/HgO). The two-electrode system was configured as two identical self-supporting nickel foam electrodes (effective geometric area: 1 cm × 0.5 cm). The electrolyte solutions for HER and OER were 1.0 M KOH. The electrolyte solution of HMFOR was 1.0 M KOH + 300 mM HMF.

The following electrochemical tests were all performed on the CHI 660D. A three-electrode system was employed. Linear sweep voltammetry (LSV) curves were tested at a sweep rate of 5 mV s^{-1}, and cyclic voltammetry (CV) activations were required before the tests to obtain stable curves. Tafel slopes were calculated from the strong polarization regions of the LSV curves according to the Tafel formula: $|\eta| = a + b \log |j|$, where b is the Tafel slope, while η, a, and j are the overpotential, constant, and current density, respectively. Electrochemical impedance spectroscopy (EIS) tests were performed at a given potential in a frequency range of 100 kHz to 0.1 Hz. The charge transfer resistance (R_{ct}) and system resistance (R_s) can be obtained by fitting the EIS data. The CV curves (60, 50, 40, 30, 20, and 10 mV s^{-1}) tested in non-Faradaic zones were used to calculate double-layer capacitance (C_{dl}). Electrochemical surface areas (ECSAs) were calculated based on the equation: ECSAs = C_{dl}/C_s, where C_s is the specific capacitance, which is 0.49 mF cm^{-2} for a piece of bare nickel foam with a geometry of 1 cm × 0.5 cm, and the details of the calculation of C_s have been presented in our previous work [38]. Faradaic efficiency (FE) for hydrogen and oxygen production were tested by the drainage gas collection method [39].

The following electrochemical tests were all performed on the PRINCETON APPLIED RESEARCH. (I) A three-electrode system was employed. The long-term stability of HER and OER was tested by chronoamperometry at −0.985 and 0.580 V (vs. Hg/HgO) to record the current-time curves, respectively. Operando EIS measurements were carried out at various potentials (frequency range: 100 kHz - 0.1 Hz; amplitude: 5 mV). (II) A two-electrode system was employed. The electrocatalytic performance of HER coupled with OER was tested when the electrolyte solution was 1.0 M KOH. The electrocatalytic performance of HER coupled with HMFOR was tested when the electrolyte solution was 1.0 M KOH + 300 mM HMF.

All test potentials (vs. Hg/HgO) were converted to potentials relative to the reversible hydrogen electrode (RHE) based on the formula: E (vs. RHE) = E (vs. Hg/HgO) + 0.0591 × pH + 0.098. The overpotential (η_j) at a certain current density (j) was calculated based on the formula: η_j = |E (vs. RHE) - E_{eq} (vs. RHE)|, where E_{eq} is the equilibrium electrode potential (0 and 1.23 V$_{RHE}$ for HER and OER, respectively). Unless otherwise stated, all LSV curves were iR-corrected based on the formula: $E_{corrected} = E_{measured} - iR_s$.

Turnover frequencies (TOFs) of NF/Co$_4$N and NF/Co$_4$N@CeO$_2$ were calculated based on the formula [38]: $TOF = I/(xFn)$, where I (A) is the current, x represents the number of electrons required to generate a product molecule (x is taken as 2, 4, and 6 for HER, OER, and HMFOR, respectively), F is the Faraday constant (96485 C mol^{-1}), and n (mol) is the number of moles of active sites (assuming that all Co are active sites). Here, $n(Co)$ of the self-supporting electrodes (effective geometric area:

1 cm × 0.5 cm) can be obtained according to the ICP-OES results. For NF/Co$_4$N and NF/Co$_4$N@CeO$_2$, $n(Co)$ is 3.3×10^{-5} and 3.4×10^{-5} mol, respectively.

2.5. High performance liquid chromatography analysis

The products of HMFOR were analyzed by an Agilent Infinity 1260 liquid chromatograph equipped with an Agilent ZORBAX SB-C18 column (5 μm, 4.6 × 150 mm). Mobile phase A was methanol, mobile phase B was ammonium formate (5 mM), A/B in the mixed mobile phase was set to 3/7, the flow rate was set to 0.6 mL min^{-1}. The column temperature was set to 30 °C and each separation lasted 10 min

The electrolyte for HMFOR was used for HPLC testing. When the electrolyte was 8 mL of 1.0 M KOH + 10 mM HMF, HMF electro-oxidation was carried out at a potential of 1.425 V$_{RHE}$ using chronoamperometry, and 50 μL of electrolyte was added to 5 mL of ultrapure water when the passing charges were 0, 10, 20, 30, 40 and 46.3 C, respectively. When the electrolyte was 8 mL of 1.0 M KOH + 300 mM HMF, HMF electro-oxidation was carried out at a current of 200 mA using chronopotentiometry, and 50 μL of electrolyte was added to 5 mL of ultrapure water when the passing charges were 0, 200, 400, 600, 800, 1000, 1200 and 1390 C, respectively. 1 mL of the mixed solution was taken for HPLC testing, and the injection volume was set to 10 μL. All products were identified and quantified based on calibration curves of standard samples of known concentration.

The HMF conversion, Faradaic efficiency (FE) and product selectivity were calculated by the following equations:

$$HMF\,conversion = \frac{mole\,of\,consumed\,HMF}{mole\,of\,initial\,HMF} \times 100\%$$

$$FE = \frac{mole\,of\,produced\,product}{total\,charge\,passed/(n \times F)} \times 100\%$$

$$Selectivity = \frac{mole\,of\,certain\,product}{mole\,of\,all\,the\,detected\,products} \times 100\%$$

where n and F are the number of electron transfer for each product formation and Faraday constant (96485 C mol^{-1}), respectively. (FDCA: $n = 6$).

2.6. Density functional theory calculations

All spin-polarized density-functional theory (DFT) computations were performed using the Vienna ab initio simulation package (VASP) based on the projector augmented wave (PAW) method [40]. Electron-ion interactions were described using standard PAW potentials [41]. A plane-wave basis set was employed to expand the smooth part of the wave functions with a cutoff kinetic energy of 400 eV. For the electron-electron exchange and correlation interactions, the functional parametrized by Perdew-Burke-Ernzerhof (PBE), a form of the general gradient approximation (GGA), was used throughout [42].

To study the mechanistic chemistry of surface reactions, the surface was modelled with a slab model. A sufficiently large vacuum region of 15 Å was used to ensure the periodic images were well separated. During the geometry optimizations, the bottom atoms were fixed at the bulk position when the surface properties were calculated. In this work, the Brillouin-zone integrations were conducted using Monkhorst-Pack grids of special points with a separation of 0.06 Å^{-1} [43,44]. The H$_2$, O$_2$ and water molecules were calculated in a 15 × 15 × 15 Å^3 box. The Brillouin-zone integrations were performed using the Gamma-point-only grid. The convergence criterion for the electronic self-consistent loop was set to 10^{-4} eV. The atomic structures were optimized until the residual forces were below 0.03 eV Å^{-1}.

3. Results and discussion

## 3.1. Synthesis and characterizations

The material synthesis route is shown in Scheme 1, which includes a three-step procedure. At first, nickel foam-supported cobalt carbonate hydroxide (NF/CCH) nanosheet arrays can be obtained by hydrothermal reaction with nickel foam as substrate, cobalt nitrate hexahydrate as Co source, and urea and sodium edetate (EDTA·4Na) as additives [45]. It should be noted that the addition of EDTA·4Na can promote the formation of CCH nanosheets, which has been discussed in detail in our previous work [45]. Subsequently, CeO_2 is introduced onto the NF/CCH by impregnation method to obtain the NF/CCH@CeO_2 composite. Finally, NF/CCH@CeO_2 is converted into NF/Co_4N@CeO_2 by nitridation treatment. The content of CeO_2 is controlled by adjusting the impregnation time, and the optimal impregnation time in this work is 6 h and the corresponding final sample is noted as NF/Co_4N@CeO_2 in the following text.

The microscopic morphologies of all samples were obtained by scanning electron microscopy (SEM). As displayed in Fig. 1a, NF/CCH exhibits the structure of nanosheet arrays, and the nanosheet surfaces are smooth. And Fig. 1b illustrates the morphology of NF/CCH@CeO_2, in which nanosheet arrays can still be seen, but their surfaces become rough. Similarly, NF/CCH@CeO_2(1 h) and NF/CCH@CeO_2(12 h) also exhibit rough nanosheet morphologies, and the longer the impregnation time, the rougher the nanosheet surface (Figs. S1 and S2). The morphology of NF/Co_4N@CeO_2 is shown in Fig. 1c, and its nanosheet array structure is basically maintained, while the surface becomes rougher, which is the result of nitridation treatment. It is worth noting that compared with NF/Co_4N (Fig. S3), NF/Co_4N@CeO_2 has a more complete nanosheet morphology, which indicates that CeO_2 can play a certain structural stabilization role. In addition, the morphologies of NF/Co_4N@CeO_2(1 h) and NF/Co_4N@CeO_2(12 h) are displayed in Figs. S4 and S5, respectively, in which the nanosheets of both are relatively complete and have rough surfaces.

X-ray diffractometer (XRD) measurements were conducted to evaluate the phase composition of the synthesized samples. Taking the impregnation time of NF/CCH in cerium nitrate solution as a variable, the XRD patterns of the synthesized samples are illustrated in Fig. 1d. When the impregnation time is 0 h, the XRD peaks of the sample (NF/CCH) correspond to $Co_2(CO_3)(OH)_2$ (PDF#36–1475, PDF represents powder diffraction files) [45–47] and Ni (PDF#04–0850), where Ni peaks are derived from the NF substrate. When the impregnation time is 1 h (NF/CCH@CeO_2(1 h)), the peaks belonging to CeO_2 (PDF#43–1002) appear, indicating that CeO_2 is successfully introduced. When the impregnation time is further increased to 6 h (NF/CCH@CeO_2) and 12 h (NF/CCH@CeO_2(12 h)), the peaks belonging to CeO_2 become more obvious, indicating that more CeO_2 might be introduced. The XRD patterns of the above samples after nitridation treatment at 500 °C are shown in Fig. 1e. The peaks belonging to $Co_2(CO_3)(OH)_2$ disappear in all samples because $Co_2(CO_3)(OH)_2$ can be converted to Co_4N (PDF#15–0806) after nitridation treatment at 500 °C [48]. In addition, peaks belonging to CeO_2 (PDF#43–1002) are present in the XRD patterns of NF/Co_4N@CeO_2(1 h), NF/Co_4N@CeO_2 and NF/Co_4N @ CeO_2(12 h), indicating that these samples contain CeO_2 phase.

Transmission electron microscopy (TEM) was used to characterize the microstructure of Co_4N@CeO_2. The TEM image of Co_4N@CeO_2
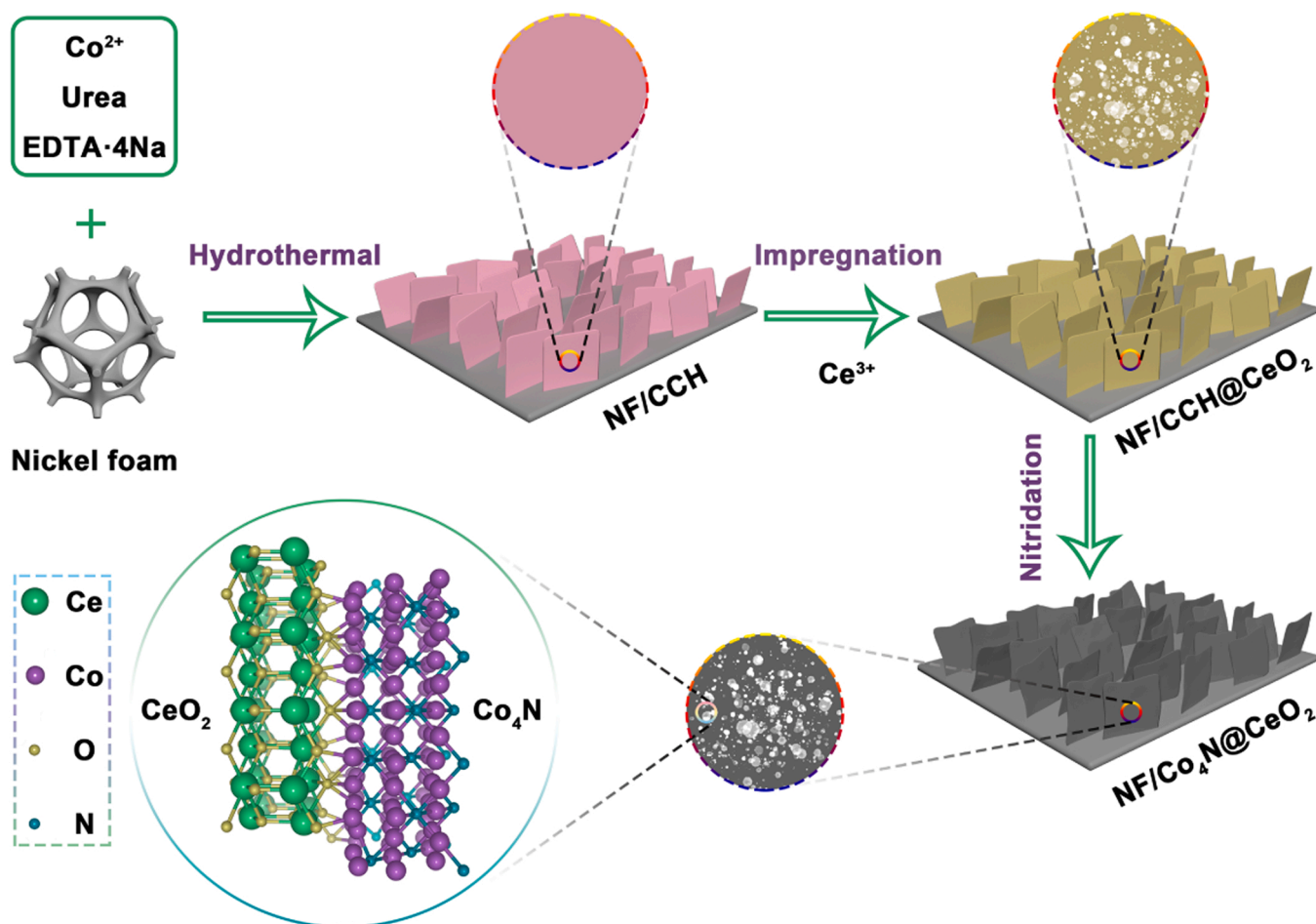
Scheme 1. Schematic illustration of the synthesis of NF/Co_4N@CeO_2.
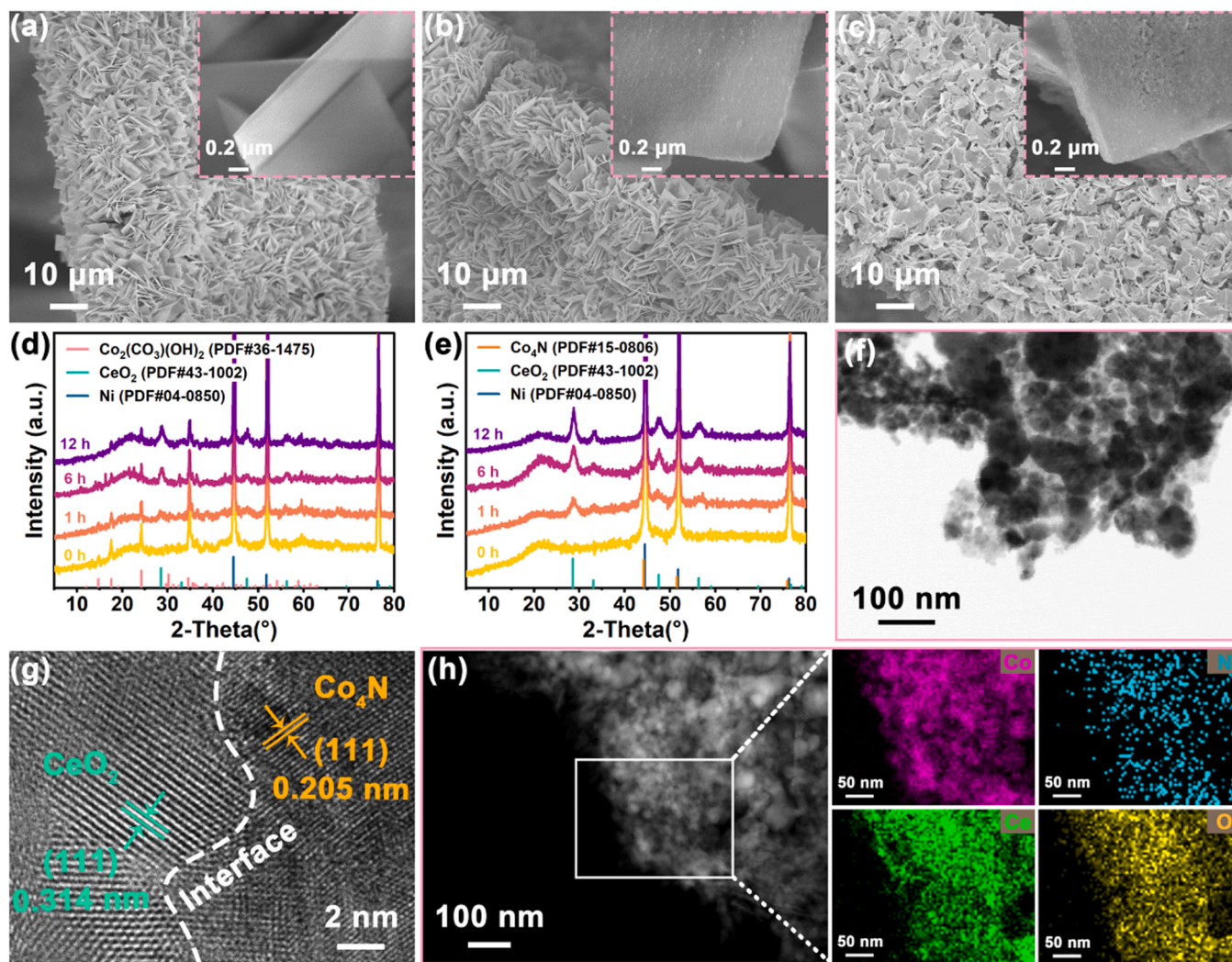
Fig. 1. SEM images of (a) NF/CCH, (b) NF/CCH@CeO$_2$, and (c) NF/Co$_4$N@CeO$_2$. (d) XRD patterns of NF/CCH, NF/CCH@CeO$_2$(1 h), NF/CCH@CeO$_2$, and NF/CCH@CeO$_2$(12 h). (e) XRD patterns of NF/Co$_4$N, NF/Co$_4$N @ CeO$_2$(1 h), NF/Co$_4$N@CeO$_2$, and NF/Co$_4$N@CeO$_2$(12 h). (f) TEM image of Co$_4$N@CeO$_2$. (g) HRTEM image of Co$_4$N@CeO$_2$. (h) STEM-EDX mapping of Co$_4$N@CeO$_2$.

again proves that it is a nanosheet structure assembled from nanoparticles (Fig. 1f). The high-resolution TEM (HRTEM) image show that Co$_4$N@CeO$_2$ has lattice fringes belonging to Co$_4$N (111) and CeO$_2$ (111) (Fig. 1g). The obvious interface between Co$_4$N and CeO$_2$ indicates the successful construction of Co$_4$N@CeO$_2$ heterostructure. Moreover, the scanning TEM-energy dispersive X-ray (STEM-EDX) mapping was utilized to determine the elemental distribution of Co$_4$N@CeO$_2$. As shown in Fig. 1h, Co, N, Ce and O elements are all present, and the distribution of each element matches the morphology of Co$_4$N@CeO$_2$ relatively well.

Inductively coupled plasma optical emission spectroscopy (ICP-OES) was applied to quantitatively analyze the Co and Ce contents in the samples. As displayed in Table S1, Ce is not detected in NF/Co$_4$N, and the atomic ratios of Co/Ce in NF/Co$_4$N@CeO$_2$(1 h), NF/Co$_4$N@CeO$_2$ and NF/Co$_4$N@CeO$_2$(12 h) are 1/0.107, 1/0.140 and 1/0.293, respectively. The above results show that the longer the impregnation time, the higher the Ce content in the final sample, which directly proves that the introduction amount of CeO$_2$ can be controlled by controlling the impregnation time.

Raman spectroscopy was used to assist in determining the chemical structure of the synthesized samples. The Raman spectra of NF/Co$_4$N, NF/Co$_4$N@CeO$_2$(1 h), NF/Co$_4$N@CeO$_2$, and NF/Co$_4$N@CeO$_2$(12 h) are shown in Fig. 2a. The strong Raman band between 600 and 700 cm^{-1} is caused by Co$_4$N [49,50]. The weak Raman band at ~505 cm^{-1}

originates from the Co-N structure in Co$_4$N or the oxygen vacancy (V$_o$) in CeO$_2$ [50]. For NF/Co$_4$N@CeO$_2$(1 h), NF/Co$_4$N@CeO$_2$, and NF/Co$_4$N@CeO$_2$(12 h), the Raman band at ~460 cm^{-1} corresponds to the F$_{2g}$ vibrational mode of cubic fluorite CeO$_2$, and the weak Raman band at ~600 cm^{-1} is connected with the existence of Ce^{3+}-V$_o$ structure [50,51].

NF/Co$_4$N@CeO$_2$ and NF/Co$_4$N were studied using X-ray photoelectron spectroscopy (XPS) to determine their surface chemical states and interfacial charges transfer. The survey XPS spectra are depicted in Fig. S6, in which the Co, O, N, and C signals can be observed, and the signal of C element may be caused by adventitious carbon contamination [52]. In addition, NF/Co$_4$N@CeO$_2$ also contains the signal of Ce element, which should originate from CeO$_2$. The high-resolution Co 2p$_{3/2}$ XPS spectra depicted in Fig. 2b are deconvoluted into four peaks of Co-Co, Co-O, Co-N, and satellite (Sat.) peaks [53–55]. For NF/Co$_4$N@CeO$_2$, Co-Co (778.7 eV) and Co-N (782.1 eV) bonds correspond to two coordination modes of Co atom in Co$_4$N, while the Co-O (780.6 eV) bond may originate from the Co-O interaction of Co$_4$N with CeO$_2$ or the surface oxidation of Co$_4$N in air [53–55]. Compared with NF/Co$_4$N, the Co-Co peak of NF/Co$_4$N@CeO$_2$ shifts to higher binding energy, which indicates that introducing CeO$_2$ can lead to the redistribution of interface charges [53,54]. Moreover, the high-resolution N 1s XPS spectra shown in Fig. 2c are deconvoluted into two peaks of Co-N and N-H bonds
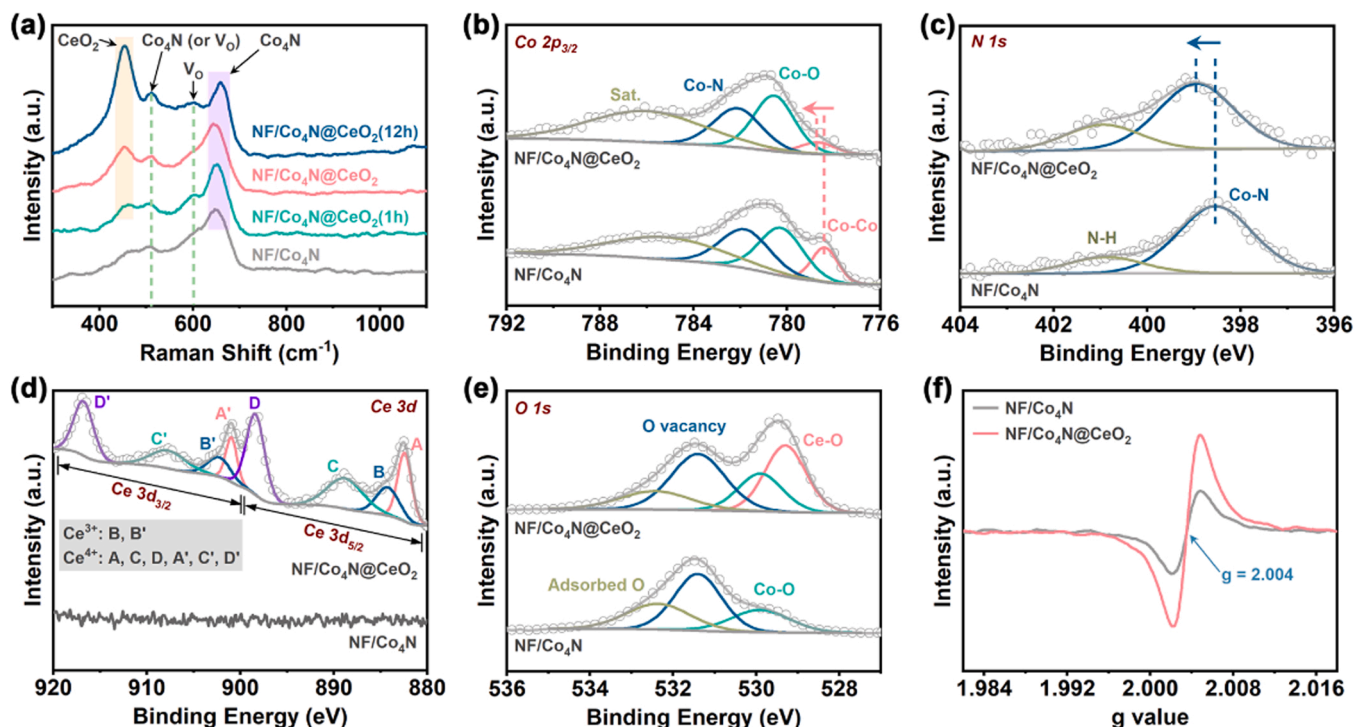
Fig. 2. (a) Raman spectra. High-resolution XPS spectra of (b) Co $2p_{3/2}$, (c) N 1s, (d) Ce 3d, and (e) O 1s for NF/Co$_4$N@CeO$_2$ and NF/Co$_4$N. (f) EPR spectra.

[48,55]. Importantly, the Co-N peak moves towards the direction of high binding energy after CeO$_2$ introduced, which again proves that the introduction of CeO$_2$ leads to the redistribution of interfacial charges [50]. In addition, in the high-resolution Ce 3d XPS spectrum of NF/Co$_4$N@CeO$_2$ (Fig. 2d), (A, C, D), (A′, C′, D′), B, and B′ peaks are assigned to Ce^{4+} 3d$_{5/2}$, Ce^{4+} 3d$_{3/2}$, Ce^{3+} 3d$_{5/2}$ and Ce^{3+} 3d$_{3/2}$, respectively [56,57]. As illustrated in Fig. 2e, the high-resolution O 1s XPS spectrum of NF/Co$_4$N is deconvoluted into three peaks of Co-O, O vacancy and adsorbed O [53,54]. Compared with NF/Co$_4$N, NF/Co$_4$N@-CeO$_2$ has one more Ce-O peak, which is derived from CeO$_2$ [53,54]. Based on the above XPS analysis, we can conclude that the introduced CeO$_2$ can lead to the redistribution of the interface charges between Co$_4$N and CeO$_2$, that is, it promotes the transfer of electrons from Co to Ce just like an "electron pump".

Oxygen vacancies in NF/Co$_4$N@CeO$_2$ and NF/Co$_4$N were also characterized using electron paramagnetic resonance (EPR) spectra. As shown in Fig. 2f, the EPR signals exhibited by NF/Co$_4$N@CeO$_2$ and NF/Co$_4$N at a g value of 2.004 indicate the presence of oxygen vacancies [58], which is mutually confirmed with the Raman results (Fig. 2a) and XPS results (Fig. 2e). Importantly, after the introduction of CeO$_2$, the EPR signal of oxygen vacancies becomes stronger, which is attributed to the abundant oxygen vacancies possessed by CeO$_2$ [54]. Notably, the presence of oxygen vacancies may promote the adsorption and migration of oxygen-containing species, thus facilitating the relevant electrochemical reactions [50,59].

3.2. Electrocatalytic performances

3.2.1. HER performance

HER performance was tested in 1.0 M KOH. Fig. 3a shows the linear sweep voltammetry (LSV) curves with iR-correction. Comparing NF/CCH and NF/CCH@CeO$_2$, it can be inferred that the introduction of CeO$_2$ slightly helps to enhance the HER activity of NF/CCH. Comparing NF/CCH@CeO$_2$ and NF/Co$_4$N @ CeO$_2$, it can be inferred that the nitridation treatment is helpful for enhancing the HER activity. And comparing NF/Co$_4$N, NF/Co$_4$N @ CeO$_2$(1 h), NF/Co$_4$N @ CeO$_2$, and NF/Co$_4$N @ CeO$_2$(12 h), it can be determined that NF/Co$_4$N @ CeO$_2$

has an optimal amount of CeO$_2$ introduction. Importantly, NF/Co$_4$N @ CeO$_2$ merely requires overpotentials of only 49 and 167 mV to supply current densities of 10 and 100 mA cm^{-2} respectively, which is better than other synthesized electrocatalysts (Fig. 3b). The outstanding HER activity of NF/Co$_4$N @ CeO$_2$ is also outperforms many other reported non-noble metal-based electrocatalysts (Table S2). In addition, the Tafel slope of NF/Co$_4$N @ CeO$_2$ (137.7 mV dec^{-1}) is lower than that of the other nitrided samples (Fig. 3c), indicating the faster reaction kinetics of NF/Co$_4$N @ CeO$_2$.

All electrochemical impedance spectroscopy (EIS) results were fitted by the equivalent circuit in the upper right corner of Fig. 3d, and the fitted EIS spectra are illustrated in Fig. 3d. The equivalent circuit consists of system resistance (R_s), charge transfer resistance (R_{ct}), and constant phase element (CPE). The R_s values are shown in Table S3 and used to perform iR compensation on the LSV curves of HER. As depicted in Fig. S7, the R_{ct} of NF/Co$_4$N @ CeO$_2$ is 2.21 Ω, which is lower than NF/Co$_4$N (4.27 Ω), NF/Co$_4$N @ CeO$_2$(1 h) (3.14 Ω), and NF/Co$_4$N @ CeO$_2$(12 h) (3.41 Ω), as well as much lower than NF/CCH (104.10 Ω) and NF/CCH@CeO$_2$ (48.31 Ω). The lowest R_{ct} value of NF/Co$_4$N @ CeO$_2$ indicates that it has the fastest charge transfer ability during the HER process.

The electrochemical surface areas (ECSAs) of all electrocatalysts were evaluated by their double-layer capacitance (C_{dl}) values obtained from the cyclic voltammetry (CV) method. CV curves at different scan rates are illustrated in Fig. S8. The calculated C_{dl} value of NF/Co$_4$N @ CeO$_2$ is 96.9 mF cm^{-2}, which is higher than that of NF/Co$_4$N, NF/Co$_4$N @ CeO$_2$(1 h), and NF/Co$_4$N @ CeO$_2$(12 h) (Fig. 3e), as well as much higher than that of NF/CCH and NF/CCH@CeO$_2$ (Fig. 3f). The highest C_{dl} value of NF/Co$_4$N @ CeO$_2$ indicates that it has the largest ECSA. In other words, NF/Co$_4$N @ CeO$_2$ possesses the largest number of active sites. In addition, to illustrate the effect of the introduction of CeO$_2$ on the specific activity of the catalyst, the ECSAs of NF/Co$_4$N and NF/Co$_4$N @ CeO$_2$ were calculated and their ECSA-normalized LSV curves were compared [60]. As shown in Fig. S9, not only the ECSA of NF/Co$_4$N @ CeO$_2$ (197.8 cm$^2_{ECSA}$) is larger than that of NF/Co$_4$N (96.1 cm$^2_{ECSA}$), but also the ECSA-normalized LSV curves show that the HER specific activity of NF/Co$_4$N @ CeO$_2$ is higher than that of
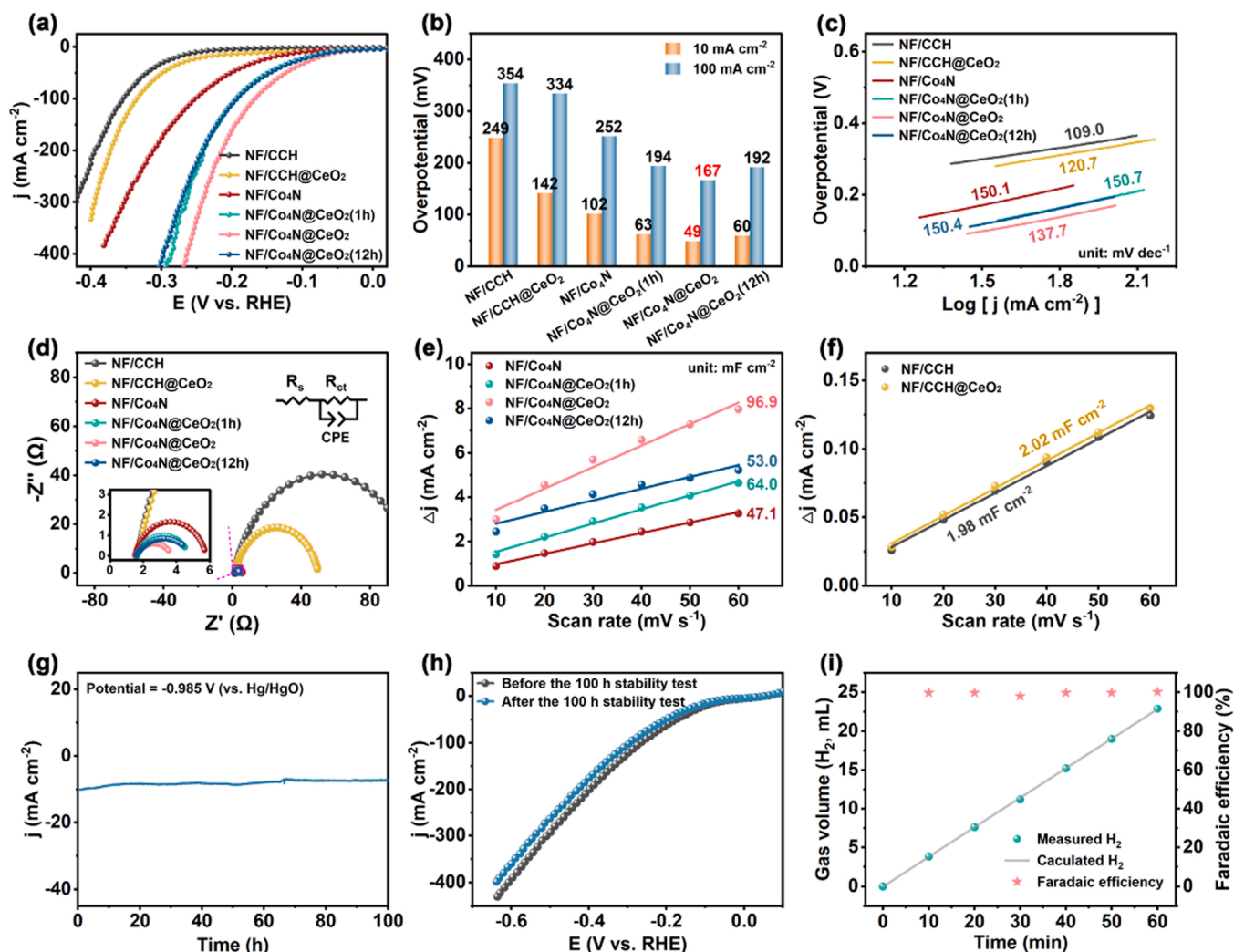
Fig. 3. (a) LSV curves, (b) overpotentials at the current densities of 10 and 100 mA cm^{-2}, (c) Tafel slopes, and (d) EIS spectra of NF/CCH, NF/CCH@CeO$_2$, NF/Co$_4$N, NF/Co$_4$N @ CeO$_2$(1 h), NF/Co$_4$N @ CeO$_2$, and NF/Co$_4$N @ CeO$_2$(12 h). (e) C$_{dl}$ values of NF/Co$_4$N, NF/Co$_4$N @ CeO$_2$(1 h), NF/Co$_4$N @ CeO$_2$, and NF/Co$_4$N @ CeO$_2$(12 h). (f) C$_{dl}$ values of NF/CCH and NF/CCH@CeO$_2$. (g) Current density-time curve of NF/Co$_4$N @ CeO$_2$ for HER in 1.0 M KOH. (h) LSV curves (without iR compensation) of NF/Co$_4$N @ CeO$_2$ before and after the 100 h HER stability test. (i) Faradaic efficiency of NF/Co$_4$N @ CeO$_2$ for hydrogen production.

NF/Co$_4$N. Moreover, the turnover frequencies (TOFs) of NF/Co$_4$N and NF/Co$_4$N @ CeO$_2$ for HER were calculated and compared to explore the effect of CeO$_2$ introduction on the intrinsic HER activity of the catalysts. As shown in Fig. S10, the TOF of NF/Co$_4$N @ CeO$_2$ is higher than that of NF/Co$_4$N at the same potential. For instance, the TOF of NF/Co$_4$N @ CeO$_2$ (1.2×10^{-2} s^{-1}) is about 3 times that of NF/Co$_4$N (3.9×10^{-3} s^{-1}) at a potential of $- 0.2$ V$_{RHE}$. Overall, the intrinsic HER activity of NF/Co$_4$N @ CeO$_2$ is higher than that of NF/Co$_4$N.

The interfacial behaviors between electrocatalyst and electrolyte were investigated by operando EIS [19,61]. The Nyquist plots of NF/Co$_4$N and NF/Co$_4$N @ CeO$_2$ at different potentials are displayed in Fig. S11a and b, respectively. As the potential gradually decreased from -0.05 to $- 0.45$ V$_{RHE}$, the Nyquist semicircular radius gradually decreased, indicating that the HER became more and more intense. In addition, at the same potential, NF/Co$_4$N @ CeO$_2$ has a smaller semicircular radius than NF/Co$_4$N, indicating that the introduced CeO$_2$ promotes the charge transfer. Moreover, the Bode plots of NF/Co$_4$N and NF/Co$_4$N @ CeO$_2$ are shown in Fig. S11c and d, respectively. The peak phase angles of the two catalysts decreased with the decrease of potential, and the peak position moved to higher frequency direction, which indicates that the decrease of potential promotes the transfer of interfacial charges and makes the control effect of mass transfer on the HER process more obvious. Furthermore, the peak phase angle of

NF/Co$_4$N @ CeO$_2$ at either potential is lower than that of NF/Co$_4$N (Fig. S11e), which again illustrates that the introduced CeO$_2$ facilitates the interfacial charge transfer.

The long-term stability of NF/Co$_4$N @ CeO$_2$ for HER was evaluated by chronoamperometry at -0.985 V (vs. Hg/HgO). During the 100 h stability test, the current density of NF/Co$_4$N @ CeO$_2$ remained basically stable (Fig. 3g). In addition, the LSV curves of NF/Co$_4$N @ CeO$_2$ before and after the 100 h stability test were acquired (Fig. 3h), and the HER activity only decreased slightly after the stability test. In summary, NF/Co$_4$N @ CeO$_2$ exhibits excellent long-term stability for HER.

A drainage gas collection method was used to measure the Faradaic efficiency (FE) of NF/Co$_4$N @ CeO$_2$ for producing H$_2$ [39]. Images of the device are displayed in Fig. S12a-b. Serial measured volumes of H$_2$ were obtained from photographs taken at different times as shown in Fig. S12c-i. And the calculated volumes of H$_2$ were acquired based on the amount of charge passed. The formula, FE = (the measured H$_2$ volume) / (the calculated H$_2$ volume) $\times$ 100 %, was applied to calculate the FE. The results are illustrated in Fig. 3i, where the FE is about 100 %, indicating that essentially no side reactions occur during the HER process.

3.2.2. OER performance

Given that the outstanding HER performance of NF/Co$_4$N @ CeO$_2$,

we then also comprehensively study its OER performance in 1.0 M KOH. Comparing the LSV curves depicted in Fig. 4a, it is clear that NF/Co$_4$N @ CeO$_2$ has the highest OER activity. In more detail, NF/Co$_4$N @ CeO$_2$ merely needs overpotentials of 263 and 325 mV to deliver current densities of 10 and 100 mA cm^{-2}, respectively, which are much lower than those of NF/Co$_4$N (303 and 372 mV), NF/CCH@CeO$_2$ (299 and 432 mV) and NF/CCH (348 and 428 mV) (Fig. 4b). Additionally, the OER specific activities of NF/Co$_4$N and NF/Co$_4$N @ CeO$_2$ were compared. The ECSA-normalized LSV curves depicted in Fig. S13 indicate that NF/Co$_4$N @ CeO$_2$ has a higher OER specific activity than NF/Co$_4$N. Furthermore, the TOF of NF/Co$_4$N @ CeO$_2$ is higher than that of NF/Co$_4$N at the same potential (Fig. S14), indicating that the introduction of CeO$_2$ enhances the intrinsic OER activity of the catalyst. Notably, compared with many reported non-noble metal-based electrocatalysts, NF/Co$_4$N @ CeO$_2$ also exhibits superior OER activity (Table S4). In addition, among all the samples shown in Fig. 4c, NF/Co$_4$N @ CeO$_2$ has the lowest Tafel slope (60.9 mV dec^{-1}), indicating it has the fastest OER kinetics.

The fitted EIS spectra are shown in Fig. 4d, where NF/Co$_4$N @ CeO$_2$ exhibits the smallest Nyquist semicircular radius. In more detail, the R$_{ct}$ of NF/Co$_4$N @ CeO$_2$ is 0.79 Ω, which is lower than NF/Co$_4$N (1.14 Ω), NF/CCH@CeO$_2$ (3.47 Ω) and NF/CCH (2.59 Ω), indicating NF/

Co$_4$N @ CeO$_2$ has the strongest charge transfer ability (Fig. S15). In addition, the R$_s$ values are shown in Table S5, which are used to iR-correct the LSV curves (OER).

To explore the effect of CeO$_2$ introduction on the interfacial behaviors between electrode and electrolyte during OER, operando EIS tests were performed on NF/Co$_4$N and NF/Co$_4$N @ CeO$_2$, respectively. Before 1.45 V$_{RHE}$, the Nyquist plots are almost straight (Fig. S16), indicating that the interfacial resistance between the two electrocatalysts and electrolyte is particularly large at low potentials [62,63]. This matches the Bode plots for both NF/Co$_4$N (Fig. 4e) and NF/Co$_4$N @ CeO$_2$ (Fig. 4f) where no arched phase angle appears before 1.45 V$_{RHE}$. When the potential rises to 1.5 V$_{RHE}$, the semicircle in the Nyquist plots (Fig. S16) and the arched phase angle in the low frequency region in the Bode plots (Fig. 4e-f) both indicate that charge transfer occurs at the electrode-electrolyte interface [19,63]. That is, OER starts to occur between 1.45 and 1.50 V$_{RHE}$, which is consistent with the result that the OER onset potentials of both NF/Co$_4$N and NF/Co$_4$N @ CeO$_2$ are between 1.45 and 1.50 V$_{RHE}$ (Fig. 4a). In the potential range from 1.50 to 1.60 V$_{RHE}$, NF/Co$_4$N @ CeO$_2$ has smaller Nyquist semicircle radius and peak phase angle than NF/Co$_4$N, which indicates that the introduced CeO$_2$ promotes the charge transfer in the OER process. Furthermore, the peak phase angles of NF/Co$_4$N and NF/Co$_4$N @ CeO$_2$ at different
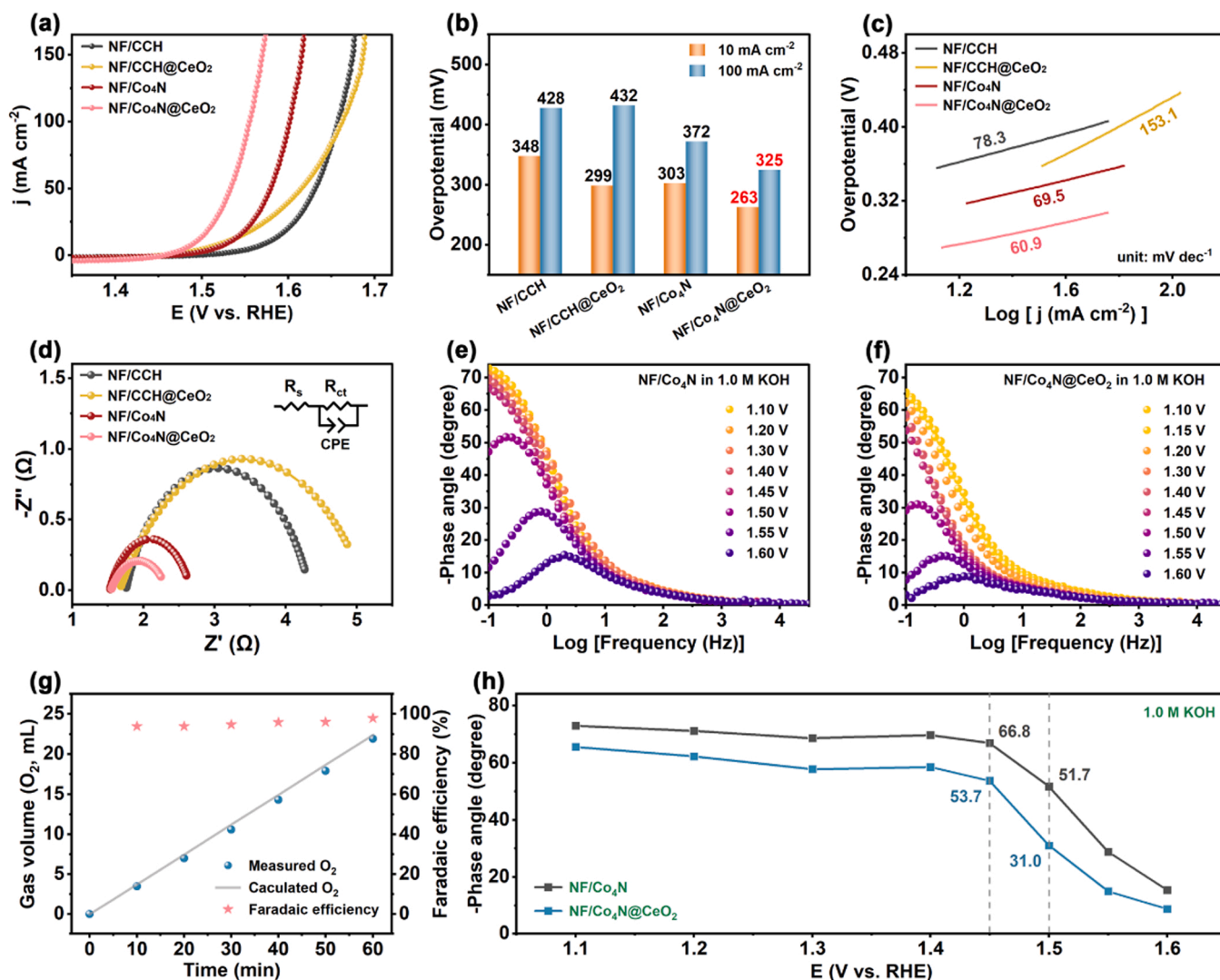
Fig. 4. (a) LSV curves, (b) overpotentials at the current densities of 10 and 100 mA cm^{-2}, (c) Tafel slopes, and (d) EIS spectra of NF/CCH, NF/CCH@CeO$_2$, NF/Co$_4$N, and NF/Co$_4$N @ CeO$_2$. Bode plots of (e) NF/Co$_4$N and (f) NF/Co$_4$N @ CeO$_2$ at various potentials in 1.0 M KOH. (g) Faradaic efficiency of NF/Co$_4$N @ CeO$_2$ for oxygen production. (h) The peak phase angles of NF/Co$_4$N and NF/Co$_4$N @ CeO$_2$ at various potentials.

potentials are shown in Fig. 4h. On the one hand, the lower phase angle of NF/Co$_4$N @ CeO$_2$ than NF/Co$_4$N indicates that the introduction of CeO$_2$ effectively reduces the interfacial resistance between catalyst and electrolyte. On the other hand, the peak phase angles of NF/Co$_4$N and NF/Co$_4$N @ CeO$_2$ decreased from 66.8 and 53.7 degrees (1.45 V$_{RHE}$) to 51.7 and 31.0 degrees (1.50 V$_{RHE}$), respectively, and the large reduction in the peak phase angle is attributed to the onset of OER, which is consistent with the results discussed above.

The FE of NF/Co$_4$N @ CeO$_2$ for oxygen production was also investigated. Fig. S17 shows the test device and measuring cylinder readings. As displayed in Fig. 4g, the measured O$_2$ production is very close to the calculated O$_2$ production. And the FE of nearly 100 % indicates that basically no other reaction occurs except OER.

The long-term stability of NF/Co$_4$N @ CeO$_2$ for OER was evaluated by chronoamperometry at 0.580 V (vs. Hg/HgO). The current density-time curve of the 100 h stability test is shown in **Fig. S18**. According to the LSV curves depicted in Fig. S19, NF/Co$_4$N @ CeO$_2$ suffered only a small loss of activity after the stability test, indicating its excellent long-term stability for OER.

Given the excellent OER and HER performance of NF/Co$_4$N @ CeO$_2$, it is promising as anode and cathode in a two-electrode system for efficient overall water splitting (OWS). The long-term stability of NF/Co$_4$N @ CeO$_2$ || NF/Co$_4$N @ CeO$_2$ for OWS was evaluated by chronoamperometry at a cell voltage of 1.565 V. The current density-time curves shown in Fig. S20, as well as the LSV curves shown in Fig. S21 (before and after the 100 h stability test) both indicate that NF/Co$_4$N @ CeO$_2$ has excellent performance stability.

3.2.3. HMFOR performance

Using HMFOR instead of OER can not only effectively reduce the energy consumption of water electrolysis for hydrogen production, but also obtain high value-added chemicals at the anode [18,19]. Therefore, we explored whether NF/Co$_4$N @ CeO$_2$ could serve as an excellent electrocatalyst for HMFOR. At first, the optimal HMF concentration was determined to be 300 mM according to the LSV curves of NF/Co$_4$N @ CeO$_2$ at different HMF concentrations (Fig. S22). Fig. 5a shows the iR-corrected LSV curves of NF/Co$_4$N @ CeO$_2$ obtained in 1.0 M KOH with and without 300 mM HMF. Importantly, the potential
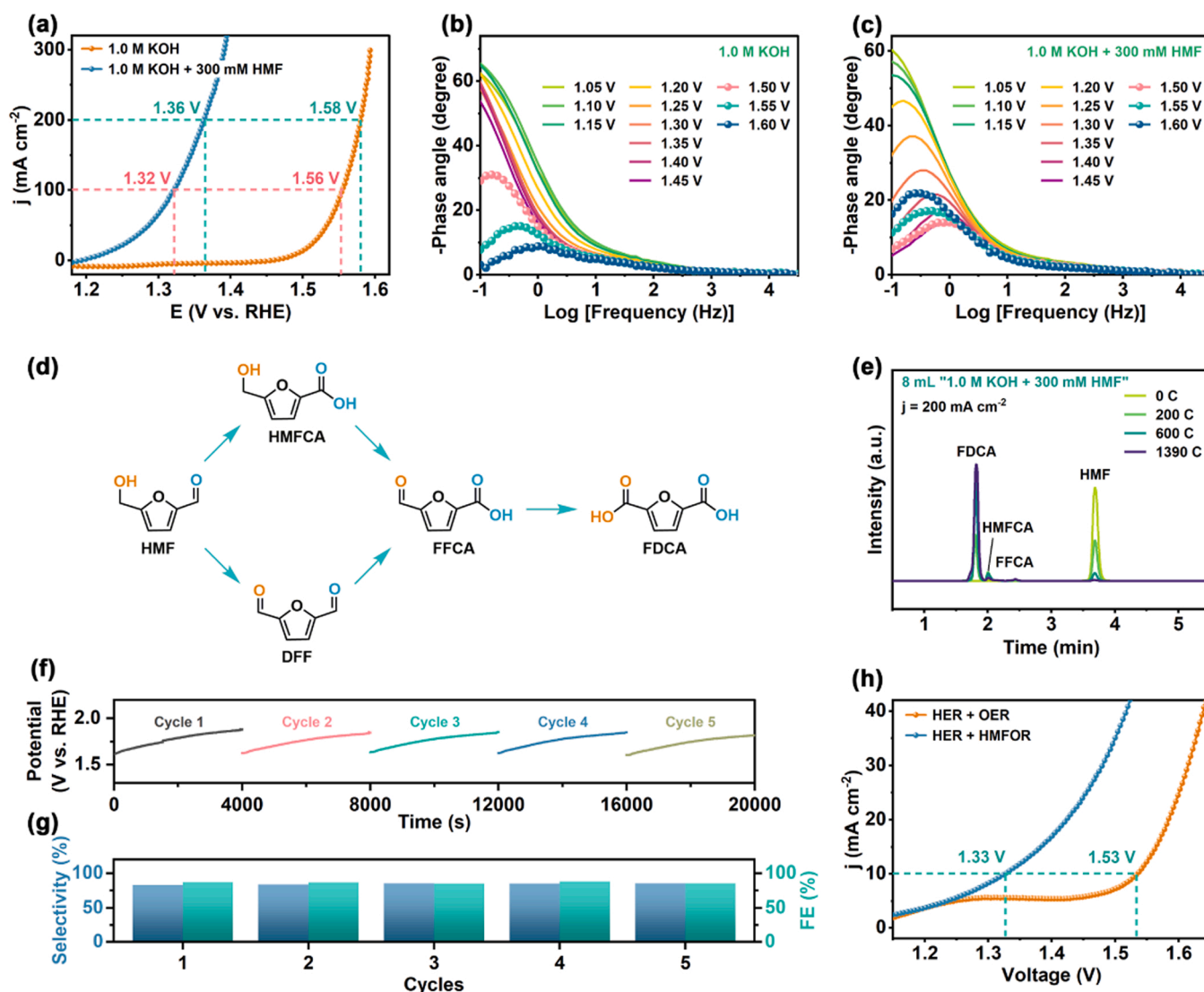
Fig. 5. (a) LSV curves of NF/Co$_4$N @ CeO$_2$ at a scan rate of 5 mV s^{-1} in 1.0 M KOH with and without 300 mM HMF. Bode plots of NF/Co$_4$N @ CeO$_2$ at various potentials in (b) 1.0 M KOH and (c) 1.0 M KOH + 300 mM HMF. (d) Two possible pathways for the oxidation of HMF to FDCA. (e) HPLC traces of the electrolyte during electrochemical HMFOR catalyzed by NF/Co$_4$N @ CeO$_2$ at a constant current of 200 mA. Electrode area: 1 cm^{-2}. (f) Potential-time curves of the HMFOR cycling test of NF/Co$_4$N @ CeO$_2$ at a constant current of 200 mA. Electrolyte: 1.0 M KOH +300 mM HMF. (g) Selectivity and FEs of NF/Co$_4$N @ CeO$_2$ for FDCA production under five successive cycles. (h) LSV curves of NF/Co$_4$N @ CeO$_2$ || NF/Co$_4$N @ CeO$_2$ at a scan rate of 5 mV s^{-1} in 1.0 M KOH with and without 300 mM HMF.

required to deliver the same current density is drastically reduced when the HMF is added. In more detail, NF/Co$_4$N @ CeO$_2$ merely requires potentials of 1.32 and 1.36 V$_{RHE}$ to deliver current densities of 100 and 200 mA cm^{-2} in 1.0 M KOH + 300 mM HMF, respectively, which are much lower than the required potentials in 1.0 M KOH (1.56 and 1.58 V$_{RHE}$).

To demonstrate the superiority of the HMFOR activity of NF/Co$_4$N @ CeO$_2$, it is necessary to compare the LSV curves of NF/Co$_4$N @ CeO$_2$ with other synthesized samples in 1.0 M KOH +300 mM HMF. As shown in Fig. S23, NF/Co$_4$N @ CeO$_2$ exhibited the higher HMFOR activity than NF/Co$_4$N, NF/CCH@CeO$_2$ and NF/CCH. Specifically, to transmit current densities of 10 and 100 mA cm^{-2}, NF/Co$_4$N @ CeO$_2$ merely needs potentials of 1.22 and 1.32 V$_{RHE}$, respectively, which are superior to NF/Co$_4$N (1.24 and 1.37 V$_{RHE}$), NF/CCH@CeO$_2$ (1.33 and 1.67 V$_{RHE}$) and NF/CCH (1.31 and 1.60 V$_{RHE}$) (Fig. S24). Furthermore, Fig. S25 shows the TOFs of NF/Co$_4$N and NF/Co$_4$N @ CeO$_2$ for HMFOR, wherein, at the same potential, the TOF of NF/Co$_4$N @ CeO$_2$ is higher than that of NF/Co$_4$N, indicating that the introduction of CeO$_2$ can improve the intrinsic HMFOR activity of the catalyst. In addition, NF/Co$_4$N @ CeO$_2$ presents a lower Tafel slope of 76.7 mV dec^{-1} than NF/Co$_4$N (118.0 mV dec^{-1}), NF/CCH@CeO$_2$ (142.2 mV dec^{-1}) and NF/CCH (143.9 mV dec^{-1}), indicating that it has the fastest HMFOR kinetics among these samples (Fig. S26).

EIS tests were also performed in 1.0 M KOH + 300 mM HMF. The fitted EIS spectra are shown in Fig. S27, where NF/Co$_4$N @ CeO$_2$ has the smallest Nyquist semicircle radius, indicating it has the smallest R$_{ct}$. In more detail, the R$_{ct}$ of NF/Co$_4$N @ CeO$_2$ is 1.83 Ω, which is superior to that of NF/Co$_4$N (3.89 Ω), NF/CCH@CeO$_2$ (9.51 Ω) and NF/CCH (13.91 Ω), indicating that NF/Co$_4$N @ CeO$_2$ has the fastest charge transfer during the HMFOR process (Fig. S28). In addition, R$_s$ values are shown in Table S6, which are applied to iR-correct the LSV curves (HMFOR).

Operando EIS was used to investigate the interfacial behaviors of NF/Co$_4$N @ CeO$_2$ in different electrolyte solutions. On the one hand, when the electrolyte is 1.0 M KOH, the Nyquist plots and corresponding Bode plots of NF/Co$_4$N @ CeO$_2$ at different potentials are shown in Fig. S29a and Fig. 5b, respectively. The OER-related interfacial charge transfer starts between 1.45 and 1.50 V$_{RHE}$ and becomes more intense with increasing potential. On the other hand, when the electrolyte is 1.0 M KOH + 300 mM HMF, the Nyquist plots and corresponding Bode plots of NF/Co$_4$N @ CeO$_2$ at different potentials are shown in Fig. S29b and Fig. 5c, respectively. When the potential is increased from 1.05 to 1.15 V$_{RHE}$, the Nyquist plots with almost straight distribution and the Bode plots without arched phase angle both indicate that no interfacial charge transfer occurs in this potential range [62,63]. When the potential is increased to 1.20 V$_{RHE}$, the appearance of the Nyquist semicircle and the arched phase angle in the low frequency region indicate that the HMFOR-related interfacial charge transfer starts between 1.15 and 1.20 V$_{RHE}$, which is consistent with the result that the HMFOR onset current appears in the potential range of 1.15–1.20 V$_{RHE}$ (Fig. 5a). When the potential is increased from 1.20 to 1.45 V$_{RHE}$, the OER do not occur, and the HMFOR-related interfacial charge transfer is enhanced with increasing potential. However, in the potential range of 1.50–1.60 V$_{RHE}$, the Nyquist semicircle radius and peak phase angle become larger with increasing potential, which is attributed to the passivation of the catalyst [64]. In addition, the peak phase angles of NF/Co$_4$N @ CeO$_2$ at different potentials are shown in Fig. S30. The addition of HMF significantly reduced the peak phase angles at lower potentials, indicating that the driving potential required for HMFOR-related interfacial charge transfer is lower.

High performance liquid chromatography (HPLC) was used to detect changes in reactants and products during the HMFOR process. First, the standard peak area-concentration curves of 5-hydroxymethylfurfural (HMF), furan-2,5-dicarbaldehyde (DFF), 5-hydroxymethyl-2-furancarboxylic acid (HMFCA), 5-formyl-2-furancarboxylic acid (FFCA) and 2,5-furandicarboxylic acid (FDCA) were determined, and the results are

shown in Fig. S31. Then, the HMF electrolysis test was performed. Similar to HMF electrolysis testing methods in some other works [18, 19], we simply tested the HMFOR performance of NF/Co$_4$N @ CeO$_2$ in electrolytes with low HMF concentrations (1.0 M KOH + 10 mM HMF). The electrolysis potential was chosen to be 1.425 V$_{RHE}$, at which essentially no OER occurred (Fig. 5a). In addition, it should be noted that the theoretical passed charge for the complete conversion of HMF to FDCA in 8 mL of the above electrolyte is about 46.3 C. The HPLC results at different passed charges are shown in Fig. S32, where in addition to the reactant (HMF) and product (FDCA) were detected, only the HMFCA intermediate was detected. The concentrations of HMF, FDCA and HMFCA under different passed charges are shown in Fig. S33. At a passed charge of 46.3 C, the HMF conversion, FDCA selectivity, and FDCA FE were 91.1 %, 93.6 %, and 84.5 %, respectively (Fig. S34). Typically, HMFOR proceeds through the HMFOR or DFF pathways (Fig. 5d). Given that only HMFOR and essentially no DFF were detected, it can be speculated that in 1.0 M KOH + 10 mM HMF, HMFOR proceeded mainly through the HMFCA pathway.

Furthermore, in order to be more suitable for practical applications, we used an electrolyte containing a high concentration of HMF (1.0 M KOH + 300 mM HMF) to study the HMFOR performance of NF/Co$_4$N @ CeO$_2$ at a constant high current (200 mA). Similarly, in 8 mL of the above electrolyte, the theoretical passed charge for complete conversion of HMF to FDCA is about 1390 C. The HPLC results and the concentration of each species at different passed charges are shown in Fig. 5e and Fig. S35, respectively. The signal of HMFCA could be detected, while the signal of DFF was basically absent, indicating that in 1.0 M KOH + 300 mM HMF, HMFOR mainly proceeded through the HMFCA pathway. In addition, under the condition of no electrolysis, the changes of various substances in the solution were also explored. Fig. S36 and S37 show the results of HPLC and the concentration of each substance at different times for the solution without electrolysis, respectively. When the time was 6950 s (corresponding to 1390 C in the case of electrolysis with a constant current of 200 mA), sufficient HMF still remained in the solution. Considering that in the case of electrolysis at a constant current of 200 mA, after 6950 s (corresponding to a passed charge of 1390 C), there is basically no HMF in the solution, thus it can be concluded that the conversion of HMF to FDCA is mainly the result of electrolysis rather than spontaneous oxidation. Additionally, the cycling stability of NF/Co$_4$N @ CeO$_2$ was also investigated. Under constant current (200 mA) electrolysis, every 4000 s was regarded as an electrolysis cycle. The potential-time curves of the cycling test are shown in Fig. 5f. Importantly, the selectivity and FE of FDCA remained stable after the cycling test, indicating the good cycling stability of NF/Co$_4$N @ CeO$_2$ (Fig. 5g). The average selectivity and average FE of FDCA were about 84.7 % and 86.5 %, respectively, in the 5 cycles of testing.

Moreover, by coupling HER and HMFOR, NF/Co$_4$N @ CeO$_2$ exhibits a more competitive activity than the OWS (HER + OER) (Fig. 5h). Specifically, to deliver a current density of 10 mA cm^{-2}, NF/Co$_4$N @ CeO$_2$ merely demands a cell voltage of 1.33 V for HER + HMFOR, while it requires a cell voltage as high as 1.53 V for HER + OER.

### 3.2.4. Characterization after electrochemical reactions

As mentioned above, NF/Co$_4$N @ CeO$_2$ exhibits excellent HER, OER and HMFOR performance. To explore the state of NF/Co$_4$N @ CeO$_2$ after those electrochemical reactions, some simple characterizations were performed after long-term stability (HER or OER) or cyclic stability (HMFOR) tests. First, the XRD patterns of NF/Co$_4$N @ CeO$_2$ before and after those electrochemical reactions did not change significantly, indicating that its crystal structure was overall stable (**Fig.** S38a). Moreover, the HRTEM images shown in Fig. S39 show that the Co$_4$N @ CeO$_2$ heterostructure remains stable to a certain extent after those stability tests. Of course, some of the nitrides may have been converted into other amorphous Co-based compounds such as CoO$_x$, which may also serve as active species [28]. In addition, the morphology

of NF/Co$_4$N @ CeO$_2$ is basically stable after those stability tests (Fig. S38g-j). Then, the surface chemical states of NF/Co$_4$N @ CeO$_2$ before and after those stability tests were characterized by XPS (Fig. S38b-f). Obviously, the surface chemical states of NF/Co$_4$N @ CeO$_2$ have changed after HER, OER, or HMFOR, which may be because the long-time electrolysis (100 h for HER/OER and 5 cycles/20,000 s for HMFOR) in a strongly alkaline environment inevitably has a certain influence on the surface of the material [53]. In order to reflect the surface chemical states of the catalyst more truly, we also performed XPS characterization of NF/Co$_4$N @ CeO$_2$ after CV activation. As shown in Fig. S40, the XPS spectra of Co 2p$_{3/2}$, N 1s, and Ce 3d basically remain stable before and after CV activation. In XPS spectra of O 1s, the Co-O/Ce-O peaks become weaker after CV activation, which may be attributed to the destruction of lattice oxygen on the catalyst surface by CV activation to a certain extent. In a word, the structure of Co$_4$N @ CeO$_2$ was maintained after the stability tests, and the surface chemical states of Co$_4$N @ CeO$_2$ after CV activation did not change much on the whole, which provided a certain guarantee for the rationality of our subsequent simulation calculation with Co$_4$N @ CeO$_2$ as the model.

3.3. Density functional theory calculations

The mechanisms of the reactions were studied in detail using density functional theory (DFT) calculations. The optimized structural models of Co$_4$N and Co$_4$N @ CeO$_2$ are illustrated in Fig. 6a-b and c-d, respectively. Differential charge density was calculated to study electronic interactions at the Co$_4$N @ CeO$_2$ heterointerface. As shown in Fig. 6e, electrons accumulate on the CeO$_2$ side of the Co$_4$N @ CeO$_2$ heterointerface, indicating some electrons transfer from Co$_4$N to CeO$_2$, which is consistent with the XPS results (Fig. 2b-c). The electronic density of states (DOS) of Co$_4$N and Co$_4$N @ CeO$_2$ are depicted in Fig. 6f, in which both have continuous electronic states across the Fermi level, indicating that they possess metal-like electron transport properties [65].
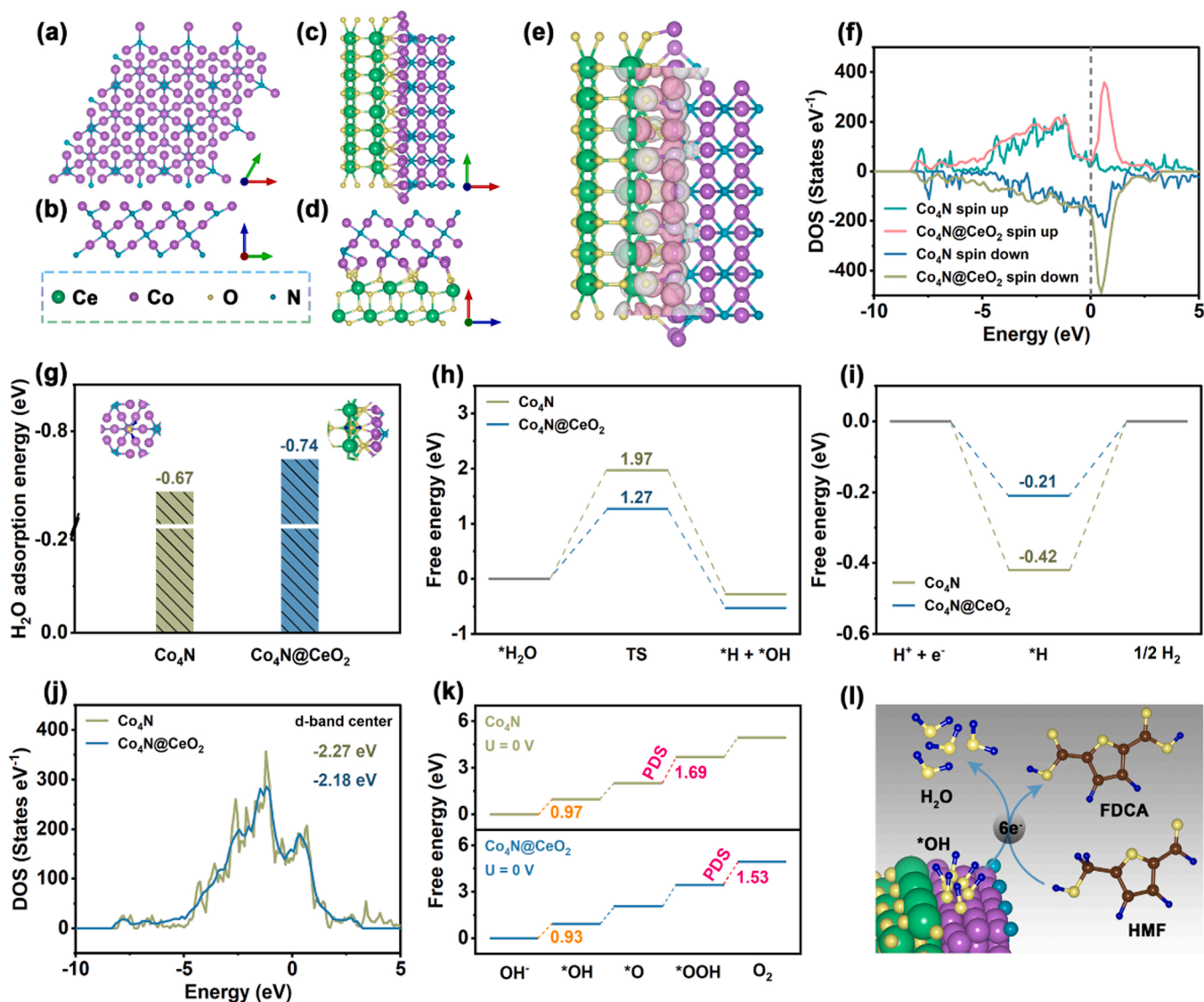
Fig. 6. Atomic structure models for (a-b) Co$_4$N and (c-d) Co$_4$N @ CeO$_2$. (e) Charge density difference profile at the Co$_4$N @ CeO$_2$ interface (light grey: electron accumulation; light pink: electron depletion). (f) Total DOS of Co$_4$N and Co$_4$N @ CeO$_2$. The Fermi level is shifted to zero. (g) The calculated free energies of H$_2$O adsorption on Co$_4$N and Co$_4$N @ CeO$_2$. (h) Free energy change during the H$_2$O dissociation process. The surface Co site in Co$_4$N and the interface Ce site in Co$_4$N @ CeO$_2$ were selected as the adsorption sites for H$_2$O. (i) Free energy change during the HER process. The surface Co site in Co$_4$N and the interface Co site in Co$_4$N @ CeO$_2$ were selected as the adsorption sites for H intermediates. (j) The ᴅ-band DOS of Co$_4$N and Co$_4$N @ CeO$_2$. (k) Free energy change during the OER process. The surface Co site in Co$_4$N and the interface Co site in Co$_4$N @ CeO$_2$ were selected as the adsorption sites for OH⁻ and O-containing intermediates. (l) Schematic diagram of HMFOR.

Importantly, $Co_4N @ CeO_2$ possesses more electronic states than Co_4N at the Fermi level, demonstrating that the introduced CeO_2 enhances the electronic conductivity of the catalyst [66].

Then for the alkaline HER process, the free energies of H_2O adsorption and dissociation should be evaluated first. A well-established H_2O adsorption and dissociation process on the $Co_4N @ CeO_2$ hetero-interface has been reported, that is, H_2O molecules first adsorb and dissociate at the Ce sites of the heterointerface, and then the generated H intermediates are transferred to the nearby Co sites [50,53]. Fig. S41 shows the H_2O adsorption and dissociation processes on the optimized structural models of Co_4N and $Co_4N @ CeO_2$. As depicted in Fig. 6g, $Co_4N @ CeO_2$ has a lower H_2O adsorption energy of -0.74 eV than Co_4N (-0.67 eV), which demonstrates that the construction of hetero-interface promotes the H_2O adsorption process. And the H_2O dissociation barriers are shown in Fig. 6 h, where the barrier of $Co_4N @ CeO_2$ (1.27 eV) is much lower than that of Co_4N (1.97 eV), indicating that the H_2O dissociation process is more inclined to occur at the heterointerface. Moreover, the Gibbs free energy change (ΔG_{*H}) of the adsorbed H intermediate should be considered for HER, and the ideal value is 0 eV [67]. **Fig. S42** shows the optimized structural models with one H intermediate adsorbed. As illustrated in Fig. 6i, the ΔG_{*H} of $Co_4N @ CeO_2$ (-0.21 eV) is much closer to 0 eV than that of Co_4N (-0.42 eV), indicating that $Co_4N @ CeO_2$ is more favorable for the HER process.

In addition, for the OER process, the D-band center of Co atom was considered first. As depicted in Fig. 6j, after the introduction of CeO_2, the D-band center of the Co atom shifts from -2.27 to -2.18 eV. According to the D-band center theory [68,69], the shift of the D-band center of the Co atom toward the Fermi level will lead to the anti-bonding state of Co-O filling with fewer electrons, thereby enhancing the adsorption of oxygen-containing species on the Co site. As shown in Fig. 6k, at U $= 0$ V, $Co_4N @ CeO_2$ has a lower OH^- adsorption barrier of 0.93 eV than Co_4N (0.97 eV), indicating that the heterointerface is more favorable for OH^- adsorption, which corroborates with the previous results based on the D-band center theory. The OER processes occurring on Co_4N and $Co_4N @ CeO_2$ are shown in Fig. S43. And the OER potential-determining step (PDS) on Co_4N is the formation of *OOH with a barrier of 1.69 eV, while the PDS changes to the formation of O_2 with a smaller barrier of 1.53 eV after CeO_2 introduced. This theoretically confirms that the construction of the $Co_4N @ CeO_2$ heterointerface is favorable for the OER process.

For the HMFOR, the HMF adsorption energies of Co_4N and $Co_4N @ CeO_2$ were calculated. Fig. S44 illustrates the structural models of Co_4N and $Co_4N @ CeO_2$ with one HMF molecule adsorbed. As described in Fig. S45, the HMF adsorption energy of $Co_4N @ CeO_2$ (-1.85 eV) is larger than that of Co_4N (-2.10 eV), demonstrating that Co_4N is more favorable for adsorbing HMF than $Co_4N @ CeO_2$. Given that the HMFOR activity of $Co_4N @ CeO_2$ is higher than that of Co_4N (**Fig. S23**), it can be speculated that the excessively strong adsorption of

HMF on the catalyst surface is not necessarily beneficial to HMFOR. Based on the previously discussed results of stronger adsorption of OH^- on the $Co_4N @ CeO_2$ surface than on the Co_4N surface (Fig. 6k), and other reports related to the HMFOR mechanism [13,70], we are more inclined to think that in the material system of this work, the adsorption strength of OH^- on the catalyst surface may affect the ease of oxidation of HMF by *OH to a certain extent. And the stronger adsorption of OH^- at the $Co_4N @ CeO_2$ heterointerface may be one of the main reasons why the HMFOR activity of $Co_4N @ CeO_2$ is higher than that of Co_4N. Finally, a simple schematic of the HMFOR occurring at the $Co_4N @ CeO_2$ heterointerface is shown in Fig. 6l. After a 6-electron transfer process, HMF is oxidized to FDCA by the adsorbed OH^- (i.e., *OH) at the heterointerface.

Finally, taking all of the above results into account, a simple schematic diagram shown in Fig. 7 is drawn to reflect how CeO_2 as an "electron pump" optimizes the interface electronic structure of $Co_4N @ CeO_2$ to promote HER, OER, and HMFOR processes. Specifically, in the $Co_4N @ CeO_2$ heterostructure, CeO_2 can act as an "electron pump", attracting electrons from the Co_4N side. Thanks to the optimization of the electronic structure of $Co_4N @ CeO_2$ interface, the adsorption of H_2O (Fig. 6g), the dissociation of H_2O (Fig. 6h), the adsorption of H intermediate (Fig. 6i), the barrier of OER PDS (Fig. 6k), and the adsorption of OH^- (Fig. 6k) can be optimized, thus promoting HER, OER and HMFOR processes.

4. Conclusions

In summary, CeO_2 was introduced into the Co_4N system as an "electron pump" to optimize the interface electronic structure of the $Co_4N @ CeO_2$ heterostructure. Experimental results show that $Co_4N @ CeO_2$ exhibits excellent multifunctional catalytic performance (HER, OER, and HMFOR). Specifically, only 49 and 263 mV over-potentials are required by $Co_4N @ CeO_2$ to transmit a current density of 10 mA cm^{-2} for HER and OER, respectively, which outperforms many reported electrocatalysts based on non-noble metal-based electrocatalysts. For HMFOR (1.0 M KOH + 300 mM HMF), $Co_4N @ CeO_2$ merely demands a low potential of 1.22 V_{RHE} to transmit a current density of 10 mA cm^{-2}, which is 273 mV lower than the potential required for OER (1.0 M KOH). Theoretical calculation results show that: (1) $Co_4N @ CeO_2$ has a low H_2O dissociation barrier and a H intermediate adsorption free energy close to zero, which is beneficial to the HER process; (2) the optimization of the electronic structure of the heterointerface changes the potential-determining step of OER and effectively reduces the potential barrier, which promotes the OER process; (3) the favorable adsorption of OH^- at the heterointerface may be the reason for its excellent HMFOR activity. The multifunctional electrocatalyst developed in this work is expected to contribute to the realization of the "carbon neutrality" goal and provide a reference for the

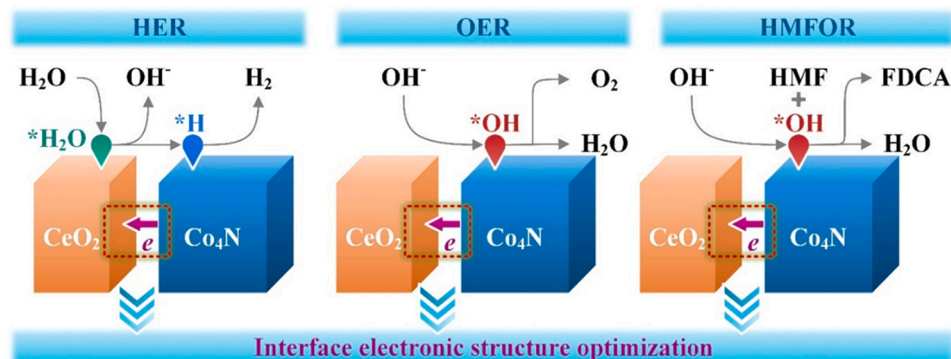**Fig. 7.** A simple schematic diagram of CeO_2 as an "electron pump" to optimize the interface electronic structure to promote HER, OER, and HMFOR. This diagram only reflects the transformation of substances, not the conservation of chemical formula.

design of other similar electrocatalysts.

CRediT authorship contribution statement

Peiyun Zhou: Conceptualization, Validation, Formal analysis, Writing – original draft. **Guangtong Hai:** Theoretical calculation. **Gongchi Zhao:** Resources. **Rushuo Li:** Resources. **Xiubing Huang:** Writing – review & editing, Supervision, Funding acquisition. **Yunfeng Lu:** Writing – review & editing, Supervision. **Ge Wang:** Writing – review & editing, Supervision, Funding acquisition.

Declaration of Competing Interest

The authors declare that they have no known competing financial interests or personal relationships that could have appeared to influence the work reported in this paper.

Data Availability

Data will be made available on request.

Appendix A. Supporting information

Supplementary data associated with this article can be found in the online version at doi:10.1016/j.apcatb.2023.122364.

References

[1] S. Chu, A. Majumdar, Opportunities and challenges for a sustainable energy future, Nature 488 (2012) 294–303, https://doi.org/10.1038/nature11475.

[2] S. Chu, Y. Cui, N. Liu, The path towards sustainable energy, Nat. Mater. 16 (2017) 16–22, https://doi.org/10.1038/nmat4834.

[3] X. Zhao, X. Ma, B. Chen, Y. Shang, M. Song, Challenges toward carbon neutrality in China: strategies and countermeasures, Resour. Conserv. Recycl. 176 (2022), 105959, https://doi.org/10.1016/j.resconrec.2021.105959.

[4] Z. Jia, B. Lin, How to achieve the first step of the carbon-neutrality 2060 target in China: the coal substitution perspective, Energy 233 (2021), 121179, https://doi.org/10.1016/j.energy.2021.121179.

[5] X. Lu, K.-h Ye, S. Zhang, J. Zhang, J. Yang, Y. Huang, H. Ji, Amorphous type FeOOH modified defective BiVO4 photoanodes for photoelectrochemical water oxidation, Chem. Eng. J. 428 (2022), 131027, https://doi.org/10.1016/j.cej.2021.131027.

[6] X. Liu, G. Liu, J. Xue, X. Wang, Q. Li, Hydrogen as a carrier of renewable energies toward carbon neutrality: State-of-the-art and challenging issues, Int. J. Miner. Metall. Mater. 29 (2022) 1073–1089, https://doi.org/10.1007/s12613-022-2449-9.

[7] Y. Wang, D. Chen, J. Zhang, M.S. Balogun, P. Wang, Y. Tong, Y. Huang, Charge relays via dual carbon-actions on nanostructured BiVO4 for high performance photoelectrochemical water splitting, Adv. Funct. Mater. 32 (2022) 2112738, https://doi.org/10.1002/adfm.202112738.

[8] Y. Wang, J. Zhang, M.S. Balogun, Y. Tong, Y. Huang, Oxygen vacancy–based metal oxides photoanodes in photoelectrochemical water splitting, Mater. Today Sustain. 18 (2022), 100118, https://doi.org/10.1016/j.mtsust.2022.100118.

[9] J. Zhang, Q. Zhang, X. Feng, Support and interface effects in water-splitting electrocatalysts, Adv. Mater. 31 (2019) 1808167, https://doi.org/10.1002/adma.201808167.

[10] F. Yang, T. Xiong, P. Huang, S. Zhou, Q. Tan, H. Yang, Y. Huang, M.S. Balogun, Nanostructured transition metal compounds coated 3D porous core-shell carbon fiber as monolith water splitting electrocatalysts: a general strategy, Chem. Eng. J. 423 (2021), 130279, https://doi.org/10.1016/j.cej.2021.130279.

[11] Y. Li, Y. Sun, Y. Qin, W. Zhang, L. Wang, M. Luo, H. Yang, S. Guo, Recent advances on water-splitting electrocatalysis mediated by noble-metal-based nanostructured materials, Adv. Energy Mater. 10 (2020) 1903120, https://doi.org/10.1002/aenm.201903120.

[12] X. Deng, M. Li, Y. Fan, L. Wang, X.-Z. Fu, J.-L. Luo, Constructing multifunctional 'Nanoplatelet-on-Nanoarray' electrocatalyst with unprecedented activity towards novel selective organic oxidation reactions to boost hydrogen production, Appl. Catal. B-Environ. 278 (2020), 119339, https://doi.org/10.1016/j.apcatb.2020.119339.

[13] Y. Yang, T. Mu, Electrochemical oxidation of biomass derived 5-hydroxymethyl-furfural (HMF): pathway, mechanism, catalysts and coupling reactions, Green. Chem. 23 (2021) 4228–4254, https://doi.org/10.1039/D1GC00914A.

[14] W. Zhang, X. Qiu, C. Wang, L. Zhong, F. Fu, J. Zhu, Z. Zhang, Y. Qin, D. Yang, C. C. Xu, Lignin derived carbon materials: current status and future trends, Carbon Res. 1 (2022) 14, https://doi.org/10.1007/s44246-022-00009-1.

[15] D. Tang, G. Lu, Z. Shen, Y. Hu, L. Yao, B. Li, G. Zhao, B. Peng, X. Huang, A review on photo-, electro- and photoelectro- catalytic strategies for selective oxidation of alcohols, J. Energy Chem. 77 (2023) 80–118, https://doi.org/10.1016/j.jechem.2022.10.038.

[16] F.W.S. Lucas, R.G. Grim, S.A. Tacey, C.A. Downes, J. Hasse, A.M. Roman, C. A. Farberow, J.A. Schaidle, A. Holewinski, Electrochemical routes for the valorization of biomass-derived feedstocks: from chemistry to application, ACS Energy Lett. 6 (2021) 1205–1270, https://doi.org/10.1021/acsenergylett.0c02692.

[17] Y. Song, W. Xie, Y. Song, H. Li, S. Li, S. Jiang, J.Y. Lee, M. Shao, Bifunctional integrated electrode for high-efficient hydrogen production coupled with 5-hydroxymethylfurfural oxidation, Appl. Catal. B-Environ. 312 (2022), 121400, https://doi.org/10.1016/j.apcatb.2022.121400.

[18] Y. Song, Z. Li, K. Fan, Z. Ren, W. Xie, Y. Yang, M. Shao, M. Wei, Ultrathin layered double hydroxides nanosheets array towards efficient electrooxidation of 5-hydroxymethylfurfural coupled with hydrogen generation, Appl. Catal. B-Environ. 299 (2021), 120669, https://doi.org/10.1016/j.apcatb.2021.120669.

[19] C. Yang, C. Wang, L. Zhou, W. Duan, Y. Song, F. Zhang, Y. Zhen, J. Zhang, W. Bao, Y. Lu, D. Wang, F. Fu, Refining d-band center in Ni0.85Se by Mo doping: a strategy for boosting hydrogen generation via coupling electrocatalytic oxidation 5-hydroxymethylfurfural, Chem. Eng. J. 422 (2021), 130125, https://doi.org/10.1016/j.cej.2021.130125.

[20] Y. Zhao, M. Cai, J. Xian, Y. Sun, G. Li, Recent advances in the electrocatalytic synthesis of 2,5-furandicarboxylic acid from 5-(hydroxymethyl)furfural, J. Mater. Chem. A 9 (2021) 20164–20183, https://doi.org/10.1039/D1TA04981J.

[21] H. Wang, J. Li, K. Li, Y. Lin, J. Chen, L. Gao, V. Nicolosi, X. Xiao, J.-M. Lee, Transition metal nitrides for electrochemical energy applications, Chem. Soc. Rev. 50 (2021) 1354–1390, https://doi.org/10.1039/D0CS00415D.

[22] Y. Li, Z. Dong, L. Jiao, Multifunctional transition metal-based phosphides in energy-related electrocatalysis, Adv. Energy Mater. 10 (2020) 1902104, https://doi.org/10.1002/aenm.201902104.

[23] Y. Huang, L. Hu, R. Liu, Y. Hu, T. Xiong, W. Qiu, M.S. Balogun, A. Pan, Y. Tong, Nitrogen treatment generates tunable nanohybridization of Ni5P4 nanosheets with nickel hydr(oxy)oxides for efficient hydrogen production in alkaline, seawater and acidic media, Appl. Catal. B-Environ. 251 (2019) 181–194, https://doi.org/10.1016/j.apcatb.2019.03.037.

[24] Y. Li, X. Wei, S. Han, L. Chen, J. Shi, MnO2 electrocatalysts coordinating alcohol oxidation for ultra-durable hydrogen and chemical productions in acidic solutions, Angew. Chem. Int. Ed. 60 (2021) 21464–21472, https://doi.org/10.1002/anie.202107510.

[25] Y. Guo, T. Park, J.W. Yi, J. Henzie, J. Kim, Z. Wang, B. Jiang, Y. Bando, Y. Sugahara, J. Tang, Y. Yamauchi, Nanoarchitectonics for transition-metal-sulfide-based electrocatalysts for water splitting, Adv. Mater. 31 (2019) 1807134, https://doi.org/10.1002/adma.201807134.

[26] J. Theerthagiri, S.J. Lee, A.P. Murthy, J. Madhavan, M.Y. Choi, Fundamental aspects and recent advances in transition metal nitrides as electrocatalysts for hydrogen evolution reaction: a review, Curr. Opin. Solid State Mater. Sci. 24 (2020), 100805, https://doi.org/10.1016/j.cossms.2020.100805.

[27] T. Xiong, X. Yao, Z. Zhu, R. Xiao, et al., In situ grown co-based interstitial compounds: non-3d metal and non-metal dual modulation boosts alkaline and acidic hydrogen electrocatalysis, Small 18 (2022) 2105331, https://doi.org/10.1002/smll.202105331.

[28] P. Chen, K. Xu, Z. Fang, Y. Tong, J. Wu, X. Lu, X. Peng, H. Ding, C. Wu, Y. Xie, Metallic Co4N porous nanowire arrays activated by surface oxidation as electrocatalysts for the oxygen evolution reaction, Angew. Chem. Int. Ed. 54 (2015) 14710–14714, https://doi.org/10.1002/anie.201506480.

[29] T. Wang, X. Cao, H. Qin, X. Chen, J. Li, L. Jiao, Integrating energy-saving hydrogen production with methanol electrooxidation over Mo modified Co4N nanoarrays, J. Mater. Chem. A 9 (2021) 21094–21100, https://doi.org/10.1039/D1TA05894K.

[30] N. Yao, Z. Fan, Z. Xia, F. Wu, P. Zhao, G. Cheng, W. Luo, Constructing the CoO/Co4N heterostructure with an optimized electronic structure to boost alkaline hydrogen evolution electrocatalysis, J. Mater. Chem. A 9 (2021) 18208–18212, https://doi.org/10.1039/D1TA04691H.

[31] N. Yao, P. Li, Z. Zhou, Y. Zhao, G. Cheng, S. Chen, W. Luo, Synergistically tuning water and hydrogen binding abilities over Co4N by Cr doping for exceptional alkaline hydrogen evolution electrocatalysis, Adv. Energy Mater. 9 (2019) 1902449, https://doi.org/10.1002/aenm.201902449.

[32] Z. Chen, Y. Song, J. Cai, X. Zheng, D. Han, Y. Wu, Y. Zang, S. Niu, Y. Liu, J. Zhu, X. Liu, G. Wang, Tailoring the d-band centers enables Co4N nanosheets to be highly active for hydrogen evolution catalysis, Angew. Chem. Int. Ed. 57 (2018) 5076–5080, https://doi.org/10.1002/anie.201801834.

[33] N. Yao, R. Meng, J. Su, Z. Fan, P. Zhao, W. Luo, Dual-phase engineering of MoN/Co4N with tailored electronic structure for enhanced hydrogen evolution, Chem. Eng. J. 421 (2021) 127757, https://doi.org/10.1016/j.cej.2020.127757.

[34] G. Lu, H. Zheng, J. Lv, G. Wang, X. Huang, Review of recent research work on CeO2-based electrocatalysts in liquid-phase electrolytes, J. Power Sources 480 (2020), 229091, https://doi.org/10.1016/j.jpowsour.2020.229091.

[35] X. Huang, K. Zhang, B. Peng, G. Wang, M. Muhler, F. Wang, Ceria-based materials for thermocatalytic and photocatalytic organic synthesis, ACS Catal. 11 (2021) 9618–9678, https://doi.org/10.1021/acscatal.1c02443.

[36] Y. Du, D. Liu, T. Li, Y. Yan, Y. Liang, S. Yan, Z. Zou, A phase transformation-free redox couple mediated electrocatalytic oxygen evolution reaction, Appl. Catal. B-Environ. 306 (2022), 121146, https://doi.org/10.1016/j.apcatb.2022.121146.

[37] Y. Huang, Y. Lu, Y. Lin, Y. Mao, G. Ouyang, H. Liu, S. Zhang, Y. Tong, Cerium-based hybrid nanorods for synergetic photo-thermocatalytic degradation of organic pollutants, J. Mater. Chem. A 6 (2018) 24740–24747, https://doi.org/10.1039/C8TA06565A.

[38] P. Zhou, R. Li, J. Lv, G. Zhao, X. Zhang, X. Huang, Y. Lu, G. Wang, Optimizing the electronic structure of CoN$_x$ via coupling with N-doped carbon for efficient electrochemical hydrogen evolution, J. Colloid Interface Sci. 628 (2022) 350–358, https://doi.org/10.1016/j.jcis.2022.08.081.

[39] J.J. Lv, P.P. Liu, R.S. Li, L.M. Wang, K.Y. Zhang, P.Y. Zhou, X.B. Huang, G. Wang, Constructing accelerated charge transfer channels along V-Co-Fe via introduction of V into CoFe-layered double hydroxides for overall water splitting, Appl. Catal. B-Environ. 298 (2021) 120587, https://doi.org/10.1016/j.apcatb.2021.120587.

[40] J. Hafner, Ab-initio simulations of materials using VASP: density-functional theory and beyond, J. Comput. Chem. 29 (2008) 2044–2078, https://doi.org/10.1002/jcc.21057.

[41] P.E. Blöchl, Projector augmented-wave method, Phys. Rev. B 50 (1994) 17953–17979, https://doi.org/10.1103/PhysRevB.50.17953.

[42] J.P. Perdew, K. Burke, M. Ernzerhof, Generalized gradient approximation made simple, Phys. Rev. Lett. 77 (1996) 3865–3868, https://doi.org/10.1103/PhysRevLett.77.3865.

[43] D.J. Chadi, Special points for brillouin-zone integrations, Phys. Rev. B 16 (1977) 1746–1747, https://doi.org/10.1103/PhysRevB.16.1746.

[44] J.D. Pack, H.J. Monkhorst, Special points for Brillouin-zone integrations—a reply, Phys. Rev. B 16 (1977) 1748–1749, https://doi.org/10.1103/PhysRevB.16.1748.

[45] P.Y. Zhou, R.S. Li, J.J. Lv, X.B. Huang, Y.F. Lu, G. Wang, Synthesis of CoP nanoarrays by morphological engineering for efficient electrochemical hydrogen production, Electrochim. Acta 426 (2022), 140768, https://doi.org/10.1016/j.electacta.2022.140768.

[46] J. González-López, Á. Fernández-González, A. Jiménez, Crystallization of nanostructured cobalt hydroxide carbonate at ambient conditions: a key precursor of Co3O4, Mineral. Mag. 80 (2016) 995–1011, https://doi.org/10.1180/minmag.2016.080.036.

[47] N. Rinaldi-Montes, J. González-López, Á. Fernández-González, A. Jiménez, D. Martínez-Blanco, Z. Amghouz, P. Gorria, J.A. Blanco, Lamellar Co3O4 nanoparticles recycled from synthetic cobalt carbonate: core/shell morphology and magnetic properties, Ceram. Int. 43 (2017) 10889–10894, https://doi.org/10.1016/j.ceramint.2017.05.125.

[48] Y. Liu, J. Zhang, Y. Li, Q. Qian, Z. Li, Y. Zhu, G. Zhang, Manipulating dehydrogenation kinetics through dual-doping Co3O4 electrode enables highly efficient hydrazine oxidation assisting self-powered H2 production, Nat. Commun. 11 (2020) 1853, https://doi.org/10.1038/s41467-020-15563-8.

[49] M.D. Meganathan, S. Mao, T. Huang, G. Sun, Reduced graphene oxide intercalated Co2C or Co4N nanoparticles as an efficient and durable fuel cell catalyst for oxygen reduction, J. Mater. Chem. A 5 (2017) 2972–2980, https://doi.org/10.1039/C6TA09729D.

[50] N. Yao, R. Meng, F. Wu, Z. Fan, G. Cheng, W. Luo, Oxygen-vacancy-induced CeO2/Co4N heterostructures toward enhanced pH-universal hydrogen evolution reactions, Appl. Catal. B-Environ. 277 (2020), 119282, https://doi.org/10.1016/j.apcatb.2020.119282.

[51] L. He, B. Liang, L. Li, X. Yang, Y. Huang, A. Wang, X. Wang, T. Zhang, Cerium-oxide-modified nickel as a non-noble metal catalyst for selective decomposition of hydrous hydrazine to hydrogen, ACS Catal. 5 (2015) 1623–1628, https://doi.org/10.1021/acscatal.5b00143.

[52] G. Greczynski, S. Mráz, L. Hultman, J.M. Schneider, Unintentional carbide formation evidenced during high-vacuum magnetron sputtering of transition metal nitride thin films, Appl. Surf. Sci. 385 (2016) 356–359, https://doi.org/10.1016/j.apsusc.2016.05.129.

[53] H. Sun, C. Tian, G. Fan, J. Qi, Z. Liu, Z. Yan, F. Cheng, J. Chen, C.-P. Li, M. Du, Boosting activity on Co4N porous nanosheet by coupling CeO2 for efficient

[54] M. Lu, D. Chen, B. Wang, R. Li, D. Cai, H. Tu, H. Yang, Y. Zhang, W. Han, Boosting alkaline hydrogen evolution performance of Co4N porous nanowires by interface engineering of CeO2 tuning, J. Mater. Chem. A 9 (2021) 1655–1662, https://doi.org/10.1039/D0TA08347J.

[55] X. Song, L. Zhao, C. Luo, X. Ren, X. Wang, L. Yang, Q. Wei, Bioactivity-protective electrochemiluminescence sensor using CeO2/Co4N heterostructures as highly effective coreaction accelerators for ultrasensitive immunodetection, Sens. Actuators B Chem. 355 (2022), 131158, https://doi.org/10.1016/j.snb.2021.131158.

[56] Y. Li, W. Luo, D. Wu, Q. Wang, J. Yin, P. Xi, Y. Qu, M. Gu, X. Zhang, Z. Lu, Z. Zheng, Atomic-level correlation between the electrochemical performance of an oxygen-evolving catalyst and the effects of CeO2 functionalization, Nano Res. 15 (2022) 2994–3000, https://doi.org/10.1007/s12274-021-3931-9.

[57] Y. Li, X. Zhang, Z. Zheng, CeO2 functionalized cobalt layered double hydroxide for efficient catalytic oxygen-evolving reaction, Small 18 (2022) 2107594, https://doi.org/10.1002/smll.202107594.

[58] J. Yin, Y. Li, F. Lv, Q. Fan, Y.-Q. Zhao, Q. Zhang, W. Wang, F. Cheng, P. Xi, S. Guo, NiO/CoN porous nanowires as efficient bifunctional catalysts for Zn–air batteries, ACS Nano 11 (2017) 2275–2283, https://doi.org/10.1021/acsnano.7b00417.

[59] J.J. Lv, L.M. Wang, R.S. Li, K.Y. Zhang, D.F. Zhao, Y.Q. Li, X.J. Li, X.B. Huang, G. Wang, Constructing a hetero-interface composed of oxygen vacancy-enriched Co3O4 and crystalline-amorphous NiFe-LDH for oxygen evolution reaction, ACS Catal. 11 (2021) 14338–14351, https://doi.org/10.1021/acscatal.1c03960.

[60] T. Xiong, B. Huang, J. Wei, X. Yao, R. Xiao, Z. Zhu, F. Yang, Y. Huang, H. Yang, M. S. Balogun, Unveiling the promotion of accelerated water dissociation kinetics on the hydrogen evolution catalysis of NiMoO4 nanorods, J. Energy Chem. 67 (2022) 805–813, https://doi.org/10.1016/j.jechem.2021.11.025.

[61] Z. Xiao, Y.-C. Huang, C.-L. Dong, C. Xie, Z. Liu, S. Du, W. Chen, D. Yan, L. Tao, Z. Shu, G. Zhang, H. Duan, Y. Wang, Y. Zou, R. Chen, S. Wang, Operando identification of the dynamic behavior of oxygen vacancy-rich Co3O4 for oxygen evolution reaction, J. Am. Chem. Soc. 142 (2020) 12087–12095, https://doi.org/10.1021/jacs.0c00257.

[62] H.-Y. Wang, S.-F. Hung, H.-Y. Chen, T.-S. Chan, H.M. Chen, B. Liu, In operando identification of geometrical-site-dependent water oxidation activity of spinel Co3O4, J. Am. Chem. Soc. 138 (2016) 36–39, https://doi.org/10.1021/jacs.5b10525.

[63] J. He, Y. Liu, Y. Huang, H. Li, Y. Zou, C.-L. Dong, S. Wang, Fe^{2+}-induced in situ intercalation and cation exsolution of Co80Fe20(OH)(OCH3) with rich vacancies for boosting oxygen evolution reaction, Adv. Funct. Mater. 31 (2021) 2009245, https://doi.org/10.1002/adfm.202009245.

[64] W. Chen, C. Xie, Y. Wang, Y. Zou, C.-L. Dong, Y.-C. Huang, Z. Xiao, Z. Wei, S. Du, C. Chen, B. Zhou, J. Ma, S. Wang, Activity origins and design principles of nickel-based catalysts for nucleophile electrooxidation, Chem 6 (2020) 2974–2993, https://doi.org/10.1016/j.chempr.2020.07.022.

[65] S. Zheng, T. Yu, J. Lin, H. Lou, H. Xu, G. Yang, FeP3 monolayer as a high-efficiency catalyst for hydrogen evolution reaction, J. Mater. Chem. A 7 (2019) 25665–25671, https://doi.org/10.1039/C9TA09985A.

[66] H. Xue, A. Meng, H. Zhang, Y. Lin, Z. Li, C. Wang, 3D urchin like V-doped CoP in situ grown on nickel foam as bifunctional electrocatalyst for efficient overall water-splitting, Nano Res. 14 (2021) 4173–4181, https://doi.org/10.1007/s12274-021-3359-2.

[67] J.K. Nørskov, T. Bligaard, A. Logadottir, J.R. Kitchin, J.G. Chen, S. Pandelov, U. Stimming, Trends in the exchange current for hydrogen evolution, J. Electrochem. Soc. 152 (2005) J23–J26, https://doi.org/10.1149/1.1856988.

[68] B. Hammer, J.K. Norskov, Why gold is the noblest of all the metals, Nature 376 (1995) 238–240, https://doi.org/10.1038/376238a0.

[69] J.K. Nørskov, F. Abild-Pedersen, F. Studt, T. Bligaard, Density functional theory in surface chemistry and catalysis, Proc. Natl. Acad. Sci. U. S. A. 108 (2011) 937–943, https://doi.org/10.1073/pnas.1006652108.

[70] R. Ge, Y. Wang, Z. Li, M. Xu, S.-M. Xu, H. Zhou, K. Ji, F. Chen, J. Zhou, H. Duan, Selective electrooxidation of biomass-derived alcohols to aldehydes in a neutral medium: promoted water dissociation over a nickel-oxide-supported ruthenium single-atom catalyst, Angew. Chem. Int. Ed. 61 (2022), e202200211, https://doi.org/10.1002/anie.202200211.